

Three-dimensional forward modelling and inversion of controlled-source electromagnetic data using the edge- based finite-element method

PAULA RULFF



ACTA UNIVERSITATIS
UPSALIENSIS
2023

ISSN 1651-6214
ISBN 978-91-513-1942-1
urn:nbn:se:uu:diva-514339



UPPSALA
UNIVERSITET

Dissertation presented at Uppsala University to be publicly examined in Hambergsalen, Geocentrum, Villavägen 16, Uppsala, Friday, 8 December 2023 at 10:00 for the degree of Doctor of Philosophy. The examination will be conducted in English. Faculty examiner: Prof. Dr. Michael Becken (University of Münster).

Abstract

Rulff, P. 2023. Three-dimensional forward modelling and inversion of controlled-source electromagnetic data using the edge-based finite-element method. *Digital Comprehensive Summaries of Uppsala Dissertations from the Faculty of Science and Technology* 2331. 81 pp. Uppsala: Acta Universitatis Upsaliensis. ISBN 978-91-513-1942-1.

Electromagnetic geophysical methods are applied to investigate anomalous subsurface structures exhibiting contrasts in electrical resistivity, as for example in mineral exploration or geothermal areas. When evaluating electromagnetic data, one big challenge is to account for full three-dimensional measurement setups and subsurface scenarios. To address this challenge, this work seeks to report on the development of a three-dimensional forward modelling code for controlled-source electromagnetic data and its integration into an inversion framework to enable the computation of three-dimensional resistivity models of the subsurface.

This thesis outlines the technical details of the developed forward and inverse modelling routines and describes synthetic tests to verify their effectiveness. The implemented forward modelling routines, based on the linear edge-based finite-element formulation on tetrahedral elements, consist of a standalone code containing a goal-oriented mesh refinement option. The forward modelling code was included with several modules into an existing inversion framework. Electromagnetic field components or impedance tensors and vertical magnetic transfer functions serve as input data for the inversion. Data gradients, required for the used non-linear conjugate-gradient inversion algorithm, were implemented for all input data types. Furthermore, regularisation options were employed and tested.

The aforementioned forward and inverse modelling codes were applied for different field settings: A forward modelling study of an ore deposit in central Sweden aimed at finding an adequate receiver distribution for the field measurements. In another modelling project, the mesh design for subsurface models containing steel-cased wells was investigated. Finally, an inversion of controlled-source electromagnetic data collected on a frozen lake in Stockholm for a tunnel-project complemented previously obtained two-dimensional resistivity models with a three-dimensional model.

The benefit of the presented research is twofold: First, the new modules added to the inversion framework can be used by the academic community to obtain improved resistivity models. Second, the reported models and field settings provide detailed information for measurement design, meshing of three-dimensional domains and local resistivity distributions of the subsurface allowing to answer geological, hydrological and geotechnical questions of selected field sites.

Keywords: Applied geophysics, Controlled-source electromagnetics, Numerical modelling, Finite-element method, Geophysical inversion

Paula Rulff, Department of Earth Sciences, Geophysics, Villav. 16, Uppsala University, SE-75236 Uppsala, Sweden.

© Paula Rulff 2023

ISSN 1651-6214

ISBN 978-91-513-1942-1

URN urn:nbn:se:uu:diva-514339 (<http://urn.kb.se/resolve?urn=urn:nbn:se:uu:diva-514339>)

Dedicated to my late grandparents

List of papers

This thesis is based on the following papers, which are referred to in the text by their Roman numerals.

- I **Rulff, P.**, Buntin, L.M. & Kalscheuer, T. (2021) Efficient goal-oriented mesh refinement in 3-D finite-element modelling adapted for controlled source electromagnetic surveys. *Geophys. J. Int.*, Volume 227, Issue 3, Pages 1624-1645,
<https://doi.org/10.1093/gji/ggab264>
- II Castillo-Reyes, O., **Rulff, P.**, Schankee Um, E. & Amor-Martin, A. (2023) Meshing strategies for 3d geo-electromagnetic modelling in the presence of metallic infrastructure. *Computational Geosciences*,
<https://doi.org/10.1007/s10596-023-10247-w>
- III **Rulff, P.**, Kalscheuer, T., Bastani, M. & Zbinden, D. (2023) Three-dimensional electromagnetic inversion of transfer function data from controlled sources. *Geophysical Prospecting*, manuscript under review
- IV **Rulff, P.** & Kalscheuer, T. (2023) A comparison between controlled-source electromagnetic field components and transfer functions as input data for three-dimensional non-linear conjugate gradient inversion. *Geophysical Prospecting*, submitted manuscript

Reprints were made with permission from the publishers.

Additional refereed journal publication not included in the thesis:

Rulff, P., Weckmann, U., Kalscheuer, T., Willkommen, G., Buntin, L.M & Platz, A. (2023) Imaging mofette structures in the Ohře (Eger) Rift System, Czech Republic, using radio-magnetotelluric data. *Results in Geophysical Sciences*, manuscript under review

Contributions

According to the Contributor Roles Taxonomy (CRediT), I contributed to the papers by:

- I Conceptualisation, Data curation, Formal analysis, Investigation, Methodology, Software, Validation, Visualisation, Writing - original draft, Writing - review & editing
- II Conceptualisation, Investigation, Methodology, Software, Visualisation, Writing - original draft, Writing - review & editing
- III Conceptualisation, Data curation, Formal analysis, Investigation, Methodology, Software, Validation, Visualisation, Writing - original draft, Writing - review & editing
- IV Conceptualisation, Data curation, Formal analysis, Investigation, Methodology, Software, Validation, Visualisation, Writing - original draft, Writing - review & editing

Contents

1	Introduction	15
2	Theoretical background	18
2.1	Electric and magnetic properties of rocks	18
2.2	Maxwell's equations	20
2.3	Controlled-source electromagnetics	22
2.4	3-D forward modelling	26
2.4.1	Boundary value problem	27
2.4.2	Finite-element formulation	28
2.4.3	Meshing and mesh refinement	29
2.5	3-D inversion	31
2.5.1	Non-linear inversion methods	31
2.5.2	Non-linear conjugate-gradient inversion	33
3	Implementation	34
3.1	Forward modelling code	34
3.2	Inversion code	41
3.2.1	Computation of data gradients	42
3.2.2	Model regularisation for tetrahedral meshes	48
3.2.3	Lagrange multiplier	50
3.2.4	Source locations	51
4	Summary of papers	54
4.1	Paper I Efficient goal-oriented mesh refinement in 3-D finite-element modelling adapted for controlled source electromagnetic surveys	54
4.1.1	Motivation	54
4.1.2	Summary	54
4.1.3	Remarks	56
4.2	Paper II Meshing strategies for 3-D geo-electromagnetic modelling in the presence of metallic infrastructure	57
4.2.1	Motivation	57
4.2.2	Summary	57
4.2.3	Comment	58

4.3 Paper III	
Three-dimensional electromagnetic inversion of transfer function data from controlled sources	59
4.3.1 Motivation	59
4.3.2 Summary	59
4.3.3 The field site	62
4.4 Paper IV	
A comparison between controlled-source electromagnetic field components and transfer functions as input data for three-dimensional non-linear conjugate gradient inversion	64
4.4.1 Motivation	64
4.4.2 Summary	64
4.4.3 Remarks	66
5 Conclusions and outlook	67
6 Plain language summary	69
7 Sammanfattning - Swedish summary	70
8 Zusammenfassung - German summary	71
9 Acknowledgements	73
References	75

Abbreviations

1-D	One-dimensional
2-D	Two-dimensional
3-D	Three-dimensional
COO	COOrdinate sparse matrix format
CSR	Complex Sparse Row matrix format
BC	Boundary Conditions
BVP	Boundary Value Problem
CSEM	Controlled-Source Electromagnetic
DC	Direct Current
DOF	Degrees of Freedom
EM	ElectroMagnetic
ERT	Electrical Resistivity Tomography
FE	Finite-Element
FEM	Finite-Element Method
HED	Horizontal Electric Dipole
HMD	Horizontal Magnetic Dipole
MT	MagnetoTelluric
MPI	Message Passing Interface
MUMPS	MUltifrontal Massively Parallel sparse direct Solver
OpenMP	Open Multi-Processing
PARDISO	PARrallel DIrect SOLver
PEC	Perfect Electric Conductor
RHS	Right-Hand Side
RMT	Radio-MagnetoTelluric
SOE	System Of Equations
SEM	Spectral Element Method
VMTF	Vertical Magnetic Transfer Function
w.r.t.	with respect to

Symbols

A	system matrix	-
B	magnetic flux density	[T] = [Wb/m ²]
b	RHS of BVP	-
C_d	data covariance matrix	-
C_m	model regularisation matrix	-
c	RHS of adjoint problem	-
d^{obs}	observed data vector	-
D	electric flux density	[C/m ²]
D	sounding depth	[m]
e	Euler's number or element	-
E	electric field or solution vector of BVP	[V/m]
$\tilde{E}_x, \tilde{E}_y, \tilde{E}_z$	electric field components	[V/m]
f	frequency	[Hz]
F(m)	simulated data vector	-
H	magnetic field	[A/m]
$\tilde{H}_x, \tilde{H}_y, \tilde{H}_z$	magnetic field components	[A/m]
h	edge length	[m]
i	imaginary unit or element index	-
J	sensitivity matrix	-
J_{el}	electric current density	[A/m ²]
J_p	impressed current density	[A/m ²]
j	edge index	-
k	iteration count	-
L	smoothness matrix	-
L	linear interpolation function	-
l	edge index	-
M	magnetisation	[A/m ²]
M	number of elements	-
m	model vector	-
N	Nédélec basis function	-
N	number of nodes	-
\hat{n}	normal vector	-
n	data count	-
P_p	impressed polarisation	[C/m ²]
q	volume electric charge density	[C/m ³]
r	source-receiver distance	[m]
S^e	surface of an element	[m ²]
T	VMTF	-
t	time or element index	[s] or -

u	data uncertainty	-
V^e	volume of an element	[m ³]
W	solution vector of adjoint problem	-
w	weighting matrix	-
Z	impedance tensor	[V/A]
δ	plane-wave skin depth	[m]
ϵ	dielectric permittivity	[F/m]
ϵ_0	vacuum dielectric permittivity	[F/m]
ϵ_r	relative dielectric permittivity	-
η	shape function	-
κ_ϵ	electric susceptibility	-
κ_μ	magnetic susceptibility	-
λ	Lagrange multiplier	-
μ	magnetic permeability	[H/m]
μ_0	vacuum magnetic permeability	[H/m]
μ_r	relative magnetic permeability	-
Φ	objective function	-
ρ	electrical resistivity	[Ωm]
σ	electrical conductivity	[S/m]
ω	angular frequency	[rad/s]
Ω	computational domain	-

Bold symbols and normal symbols denote vectors or matrices and scalar quantities, respectively.

1. Introduction

Human society has a tremendous demand for resources, such as energy, drinking water and minerals. However, resource exploration is, due to various reasons, a challenging task (e.g. Ghorbani et al., 2023; Jones, 2023). For instance, the environmental impact during raw material extraction ought to be minimised (European Environment Agency, 2021). Yet, the availability of the critical materials required to decrease our impact on climate change while maintaining our living standards has to be insured. The important resources reside predominantly below the surface. Based on their physical properties, they can be detected with geophysical methods.

Electromagnetic (EM) geophysical methods can be used to investigate the electrical resistivity distribution of the subsurface (Nabighian, 1987). Among them, frequency-domain controlled-source electromagnetic (CSEM) methods have been developed into routinely applied tools for marine exploration purposes (Constable, 2010). More recently, the interest in applying the CSEM method on land with purely surface based setups, borehole instruments or semi-airborne methods also increased (e.g. Grayver et al., 2014; Tietze et al., 2015; Streich, 2016; Schaller et al., 2018; Patzer et al., 2019; Tietze et al., 2019; Becken et al., 2020; Castillo-Reyes et al., 2021). Nowadays, CSEM is an established method to be applied, alongside other geophysical methods, for exploration, but also for environmental engineering tasks on land.

To obtain resistivity models of the subsurface at land-based exploration sites, forward modelling and inversion approaches are required. They should account for three-dimensional (3-D) variations of the surface topography, complex geology of the subsurface and advanced measurement setups. Evaluating large data sets in 3-D is a computer resource demanding task. In the last three decades, the capabilities of computers improved significantly. Therefore, a number of 3-D frequency-domain CSEM forward modelling (e.g. Avdeev et al., 1997; Schwarzbach et al., 2011; Puzyrev et al., 2013; Ansari and Farquharson, 2014; Grayver and Kolev, 2015; Castillo-Reyes et al., 2018; Rochlitz et al., 2019; Werthmüller et al., 2019; Elías et al., 2022; Liu et al., 2023) and inversion codes (e.g. Haber et al., 2004; Newman and Boggs, 2004; Mackie et al., 2007; Gribenko and Zhdanov, 2007; Commer and Newman, 2008; Plessix and Mulder, 2008; Abubakar et al., 2009; Grayver et al., 2013; Kelbert et al., 2014; Bretaudeau and Coppo, 2016; Cao et al., 2016; Heagy et al., 2017; Zhang, 2018; Long et al., 2020; Cai et al., 2021; Smirnova et al., 2023; Rochlitz et al., 2023; Zhang et al., 2023) were developed.

However, research on 3-D methods and code development is ongoing. The most challenging tasks are (i) improving the accuracy of the forward responses while minimising computational costs (e.g. Grayver and Kolev, 2015), (ii) mesh design (e.g. Oldenburg et al., 2020; Werthmüller et al., 2021), (iii) developing efficient solvers (e.g. Grayver and Kolev, 2015; Weiss et al., 2023b), (iv) handling, simulating and inverting large data sets collected over a 3-D subsurface with multiple transmitters (e.g. Auken et al., 2006; Rochlitz et al., 2023) and (v) developing methods to improve inversion results, for instance with joint inversion approaches (e.g. Moorkamp, 2017), and to assess the reliability of 3-D subsurface models (e.g. Ren and Kalscheuer, 2020). Therefore, this thesis deals with implementing, improving and further investigating 3-D forward modelling and inversion approaches for the frequency-domain CSEM method.

Major parts of the work presented in this thesis were conducted within the framework of the Smart Exploration project launched in December 2017 through the EU's Horizon2020 Research and Innovation Programme. The project aimed at developing cost-effective, environmentally friendly geophysical solutions for mineral exploration. As part of the work package 'Advanced Subsurface Imaging and Modelling' of the Smart Exploration project and as the first task in the PhD project, a 3-D CSEM forward modelling code called `elfe3D` was developed and applied to a mineral exploration scenario.

The main objectives of this thesis are concerned with 3-D CSEM forward and inverse modelling. The included papers focus on novel implementation aspects, verification of the developed codes and their application to simulate and invert data from synthetic and real-world subsurface models.

Paper I introduces the developed 3-D CSEM forward modelling code `elfe3D` including a detailed description of error estimators for goal-oriented adaptive mesh refinement customised specifically for CSEM problems. The code is based on linear edge-based finite-element (FE) approximations combined with unstructured tetrahedral meshes and a total electric field approach. It simulates electric and magnetic fields generated by extended electric or magnetic sources on a 3-D subsurface. The paper focuses on three important aspects: i) the methodology of the mesh refinement and error estimation approach, ii) the verification of the forward modelling code through comparison with a semi-analytic and a high-order FE reference solution and iii) the capabilities of the implemented mesh refinement presented on synthetic numerical examples and one real-world scenario with a measurement setup above a complex-shaped ore deposit.

Paper II shows the application of `elfe3D` and, specifically, of the mesh refinement to models that include steel-cased wells. Therefore, the code is extended to deal with perfect electric conductors (PEC) within the model domain. A PEC can be used to approximate a highly conductive steel-casing of a well. This paper is a collaborative work combining the capabilities of an external 3-D CSEM forward modelling code, `petgem` (Castillo-Reyes et al., 2018),

using higher-order approximations with the mesh refinement techniques of `elfe3D`. The most important outcomes of this work are meshing and modelling recommendations for subsurface models that include highly-conductive, small-scale geotechnical structures such as steel-cased wells.

Paper III describes the implementation of `elfe3D` into an in-house inversion framework, called *emilia* (Kalscheuer et al., 2008, 2010, 2015). A non-linear conjugate gradient (NLCG) inversion algorithm is adjusted to enable handling 3-D CSEM data sets by implementing gradient computations and regularisation options for tetrahedral meshes. Increased sensitivity close to source locations is counteracted by a weighting function in the regularisation term. Furthermore, **Paper III** demonstrates the inversion using two synthetic and one field data sets. The results reveal that the inversion reproduces the original synthetic models sufficiently well. The field data set was collected for a tunnel infrastructure project and 2-D resistivity models have been computed previously (e.g. Bastani et al., 2022). In the new 3-D resistivity model, the main features correlate well with previously obtained 2-D models.

Paper IV investigates whether the use of electric and magnetic field components or impedance tensors and vertical magnetic transfer functions (VMTF) as input data for 3-D NLCG inversion is more favourable. Using the inversion methodology developed for **Paper III**, this work compares inversions with both input data types using a simple, but practical, synthetic model. It comprises two extended, perpendicularly oriented, grounded electric sources and a receiver grid above two conductive anomalies. The results reveal that the resistivity distribution below the receiver grid including the conductive anomalies is well recovered with the transfer function data. With the field components, the true model resistivity below the source can additionally be imaged, but the overall resistivity model appears more heterogeneous and includes a stronger source signature than the resistivity model obtained by inverting transfer functions. For the studied example, the convergence behaviour of the transfer function inversion is better than that of the EM field component inversion.

The following sections are intended to make the content of **Papers I-IV** more accessible by providing important background information and implementation details. It is important to note that concepts presented in detail in one of the included papers are largely not repeated. Instead, the reader is referred to the related sections in the specific articles. Chapter 2 introduces the underlying theory of EM geophysics and the general concepts of forward modelling and inversion including the specific numerical methods used. Chapter 3 outlines details on the implementations of the forward and inverse modelling codes which have been employed during this PhD project and applied in the aforementioned papers. Chapter 4 provides comprehensive summaries of the included papers and additional remarks on these papers. In Chapter 5, the main conclusions and research outlooks of this work are given. Afterwards, short summaries of this thesis in easy accessible language are provided in English, Swedish and German.

2. Theoretical background

This chapter provides relevant theoretical background information on EM geophysics, the CSEM concept and the specific methods used for forward and inverse modelling.

2.1 Electric and magnetic properties of rocks

Geophysicists are interested in investigating the physical properties of the subsurface, i.e. the rocks. A physical property of a material quantifies how the material responds to a particular physical input. For example, the electrical conductivity (inverse resistivity) of rocks quantifies how easily electric charges can move through the rock material, if exposed to an applied electric field. EM geophysical methods are sensitive to three different rock properties: the electrical resistivity ρ [Ωm], the dielectric permittivity ε [F/m] and the magnetic permeability μ [H/m].

The electrical resistivity ρ of a subsurface material in our lithosphere is caused by the so-called conduction processes. Moving ions in electrolytic pore fluids (ionic conduction), charge accumulation at interfaces between subsurface fluids and rocks (surface conduction) or current flow through the movement of free electrons in metallic rocks (electronic conduction). Consequently, fluids and clay minerals play an important role in conduction processes (Telford et al., 1990).

The dielectric permittivity is described by $\varepsilon = \varepsilon_r \varepsilon_0$, where ε_0 is the vacuum dielectric permittivity ($\approx 8.8541878128 \times 10^{-12}$ [F/m]). $\varepsilon_r = \frac{\varepsilon}{\varepsilon_0}$ is the relative dielectric permittivity which quantifies polarisation effects in materials exposed to an external electric field (Keller, 1987) relative to the vacuum dielectric permittivity. ε_r can also be expressed in terms of the electric susceptibility $\kappa_\varepsilon = \varepsilon_r - 1$.

The magnetic permeability $\mu = \mu_r \mu_0 = (1 + \kappa_\mu) \mu_0$ measures the magnetisation of a material exposed to a magnetic field. μ_0 is the magnetic permeability of free space ($\approx 4\pi \times 10^{-7}$ [H/m]). The dimensionless relative magnetic permeability μ_r is the ratio of the magnetic permeability of a material to the free space magnetic permeability. Geoscientists tend to express this quantity using the magnetic susceptibility $\kappa_\mu = \mu_r - 1$, which is dimensionless (Reynolds, 2011).

Out of the three above mentioned properties, the electrical resistivity varies over the widest range for different rock types (Fig. 2.1). Electrical resistivity

models, in combination with geological information, can provide insights into the types and distribution of subsurface materials in a region of interest. Soils and sedimentary rocks tend to have the lowest resistivities, but their effective resistivities are strongly dependent on the proportion of pore space and the type of pore space filling. For instance, pores filled with saline water can significantly reduce the resistivity of a rock. Igneous and metamorphic rocks are characterised by higher resistivities compared to sediments. However, there are exceptions like Graphite Schists, which can be detected as strong conductors with EM imaging methods due to low-frequency polarisation rather than conduction effects (Römhild et al., 2019). Rocks, especially when having a laminated structure, can also be electrically anisotropic, i.e. their resistivity varies in different directions (Reynolds, 2011). The electrical resistivity is the main material property that can be investigated with CSEM methods. Nevertheless, it is important to include magnetic permeability and dielectric permittivity in modelling certain subsurface scenarios.

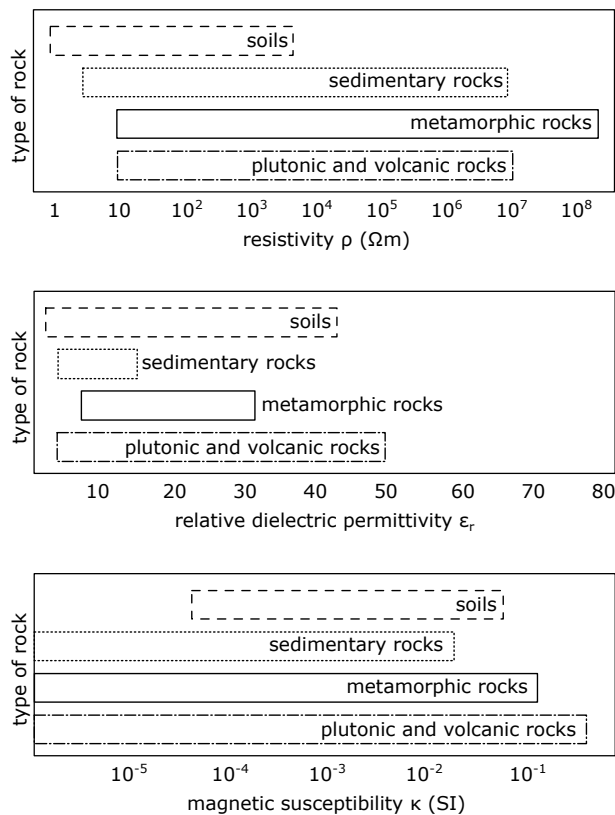


Figure 2.1. Typical ranges of resistivity, relative dielectric permittivity and magnetic susceptibility for the main rock types, compiled from Keller (1982), Telford et al. (1990) and Reynolds (2011).

2.2 Maxwell's equations

Maxwell's equations describe the static and dynamic behaviour of electric and magnetic fields and the coupling between fields (e.g. Ward and Hohmann, 1988). They also relate electric and magnetic fields to material properties. Using a time dependency of $e^{i\omega t}$, Maxwell's equations in frequency-domain can be stated as follows:

$$\nabla \times \mathbf{E} = -i\omega\mu\mathbf{H} \quad (\text{Faraday's law}) \quad (2.1)$$

$$\nabla \times \mathbf{H} = \left(\frac{1}{\rho} + i\omega\epsilon\right)\mathbf{E} + \mathbf{J}_p \quad (\text{Ampère's law}) \quad (2.2)$$

$$\nabla \cdot (\epsilon\mathbf{E}) = q \quad (\text{Gauss' law}) \quad (2.3)$$

$$\nabla \cdot \mu\mathbf{H} = 0, \quad (2.4)$$

where ω denotes the angular frequency [rad/s], \mathbf{E} the electric field [V/m], \mathbf{H} the magnetic field [A/m]. \mathbf{J}_p is the impressed current density of the source, q is the volume electric charge density [C/m³] and i the imaginary unit.

Further important quantities tied to the material properties via three constitutive relations are

- the electric current density $\mathbf{J}_{el} = \frac{1}{\rho}\mathbf{E}$ [A/m²],
- the electric flux density, also called electric displacement, $\mathbf{D} = \epsilon\mathbf{E} + \mathbf{P}_p$ [C/m²], where $\epsilon\mathbf{E} = \epsilon_0\mathbf{E} + \kappa_\epsilon\epsilon_0\mathbf{E}$, with $\epsilon = \epsilon_r\epsilon_0 = (1 + \kappa_\epsilon)\epsilon_0$, originating from an induced electric polarisation $\kappa_\epsilon\epsilon_0\mathbf{E}$ and an impressed polarisation \mathbf{P}_p and,
- the magnetic flux density $\mathbf{B} = \mu_0(\mathbf{H} + \mathbf{M}_i + \mathbf{M}_r + \mathbf{M}_p)$ [Wb/m²], consisting of an induced magnetisation $\mathbf{M}_i = \kappa_\mu\mathbf{H}$, a remnant magnetisation \mathbf{M}_r and an impressed magnetisation \mathbf{M}_p .

When modelling EM field behaviour in a domain, continuity conditions across interfaces, which can be deduced from Maxwell's equations (Ward and Hohmann, 1988), have to be considered: the normal components of \mathbf{J}_{el} and \mathbf{B} and the tangential components of \mathbf{E} and \mathbf{H} are continuous across interfaces. The normal component of \mathbf{D} is discontinuous due to accumulation of a surface charge density q_s .

For low-frequency CSEM applications, the quasi-static condition that is $\omega\epsilon\rho \ll 1$ often holds. Thus, conduction effects are dominant (cf. Fig. 2.2), and polarisation effects that are described by the displacement current term ($i\omega\epsilon\mathbf{E}$ in eq. 2.2) are frequently neglected. However, this is not the case for high frequencies in combination with high resistivities. Furthermore, induced magnetisation can often be neglected, i.e. $\mu = \mu_0$. For subsurface scenarios that include magnetic features (such as ore bodies) this is however not

the case. Therefore, magnetic permeability and dielectric permittivity are included alongside electrical resistivity as variable model parameters in the forward modelling approach described in this thesis.

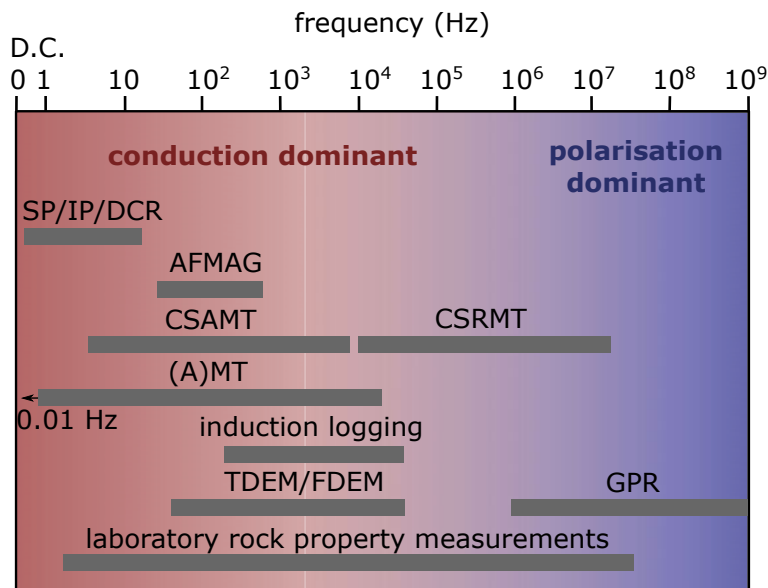


Figure 2.2. EM methods in the frequency band $0 - 10^9$ Hz used in applied geophysics, adapted from Dentith and Mudge (2014). SP: self potential, IP: induced polarisation, DCR: direct current resistivity, AFMAG: audio-frequency magnetic method, CSAMT: controlled-source audio-frequency magnetotellurics, CSRMT: controlled-source radio-frequency magnetotellurics, (A)MT: (audio-frequency) magnetotellurics, TDEM: time-domain EM, FDEM: frequency-domain EM, GPR: ground-penetrating radar.

2.3 Controlled-source electromagnetics

CSEM is an EM geophysical method and its principle is thus based on Maxwell's equations (eqs. 2.1-2.4). A time-varying source current generates a primary EM field. The source current can be produced by a transmitter aerial in form of a loop simulating a magnetic source or an extended grounded cable simulating an electric dipole or bipole (e.g. Zhdanov, 2009). Alongside the primary electric field, a secondary electric field drives secondary currents in the conductive subsurface. These secondary currents generate secondary magnetic fields that are, in turn, inducing secondary electric fields. Secondary currents can also be generated due to surface charges at interfaces between materials that differ in their electric material properties. The primary and secondary EM fields, i.e. the total EM field, are recorded at a sounding unit, i.e. a receiver (Fig. 2.3). The measured fields contain information on the electric and magnetic material property distribution in the subsurface.

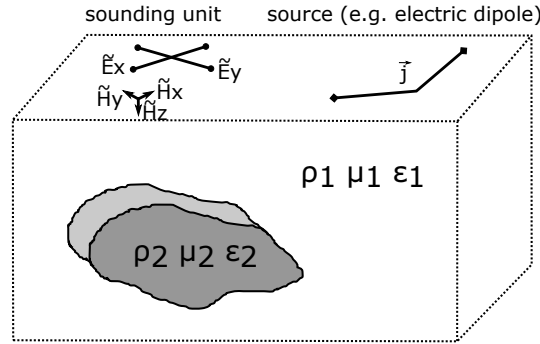


Figure 2.3. Schematic illustration of a ground-based CSEM measurement setup above a subsurface anomaly exhibiting differences in rock properties, namely electrical resistivity ρ , dielectric permittivity ϵ and magnetic permeability μ , compared to the surrounding half space.

In standard, low-frequency land-based CSEM applications, two horizontal electric (\tilde{E}_x , \tilde{E}_y) and three orthogonal magnetic (\tilde{H}_x , \tilde{H}_y , \tilde{H}_z) field components are measured at the surface (Fig. 2.3). A transmitter generates a signal in a frequency range from about 0.1 Hz to 10 kHz. Note, that it is also possible to measure the magnetic field components in the air (e.g. Becken et al., 2020) and to obtain the vertical electric (\tilde{E}_z) field component utilising boreholes (Patzner et al., 2019). The possible depth of investigation typically ranges from a few tens of metres to a few kilometres depending on the material properties of the subsurface, the frequency content of the transmitted signal and the transmitter-receiver separation.

The EM fields are measured in time domain and processed via time-series segmentation, filtering, tapering and Fourier transformation into EM fields in

frequency domain. Using least-squares methods, transfer functions can be computed at individual frequencies. Measured data always contain uncertainties arising from noise, instrument-related issues and imperfect station setup in the field. Therefore, data uncertainties are estimated during a data processing procedure.

One approach for evaluating CSEM data is to invert the individual measured EM field components normalised with the source currents at distinct frequencies (Becken et al., 2020). For CSEM measurements, one can define different zones (Zonge and Hughes, 1991) based on source-receiver separation r and the plane-wave skin depth

$$\delta = \left(\sqrt{\frac{\omega\mu}{2\rho}} \right)^{-1} \quad (2.5)$$

that describes the distance over which the amplitude of an impinging EM field is reduced by a factor $1/e$ for quasi-static conditions. It is often utilised to estimate the depth of investigation for plane-wave EM methods.

The above mentioned zones (Fig. 2.4) are

- the near-field zone: close to source, $r \ll \delta$, direct-current (DC) limit,
- the transition zone: $r \approx \delta$ and
- the far-field zone: far away from source, $r \gg \delta$.

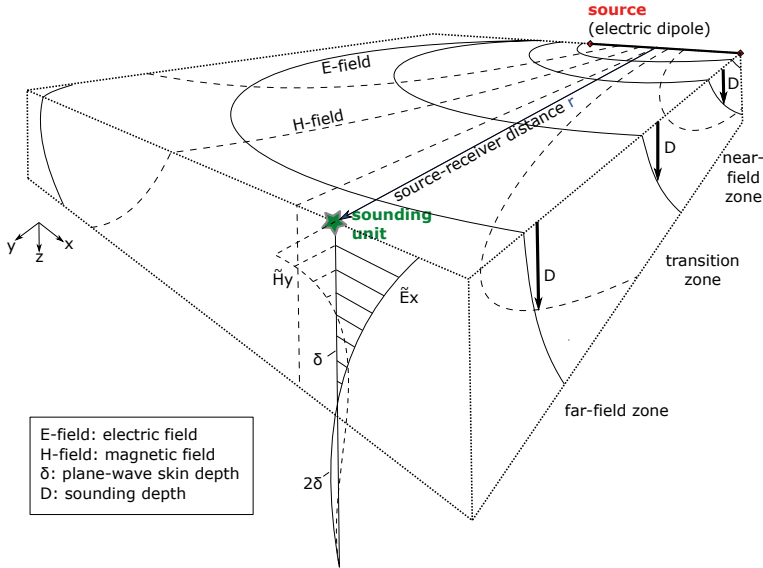


Figure 2.4. Schematic illustration of the EM field behaviour in near-field, transition and far-field zones for a ground-based CSEM measurement with an electric bipole source and a receiver site (sounding unit). Modified after Zonge and Hughes (1991).

The electric and magnetic fields in a homogeneous half space measured at a receiver site located in the different zones behave as follows (Zonge and Hughes, 1991):

- Near-field zone: EM fields are predominantly dependent on the measurement geometry. Only the electric field holds information on the subsurface. As for electrical resistivity tomography (ERT) methods, the sounding depth D increases for larger source-receiver separation.
- Transition zone: The EM fields are functions of measurement geometry, electric and magnetic properties of the subsurface and frequency.
- Far-field zone: The EM fields approximate plane waves. As for magnetotelluric (MT) methods, the sounding depth D depends on frequencies and electric and magnetic properties of the subsurface.

Due to the linearity of Maxwell's equations (cf. Sec. 2.2), one can relate the electric and magnetic field components in frequency domain through

$$\begin{bmatrix} \tilde{E}_x \\ \tilde{E}_y \\ \tilde{H}_z \end{bmatrix} = \begin{bmatrix} Z_{xx} & Z_{xy} \\ Z_{yx} & Z_{yy} \\ T_x & T_y \end{bmatrix} \begin{bmatrix} \tilde{H}_x \\ \tilde{H}_y \end{bmatrix}. \quad (2.6)$$

The impedance tensor

$$\mathbf{Z} = \begin{bmatrix} Z_{xx} & Z_{xy} \\ Z_{yx} & Z_{yy} \end{bmatrix} \quad (2.7)$$

and the vertical magnetic transfer function (VMTF)

$$\mathbf{T} = \begin{bmatrix} T_x & T_y \end{bmatrix} \quad (2.8)$$

are often used to evaluate plane-wave EM methods. However, impedance tensors and VMTF can also be uniquely defined for CSEM, as long as two independent source polarisations are excited (Li and Pedersen, 1991; Bretaudeau and Coppo, 2016). The method is called "Tensor CSAMT" (Zonge and Hughes, 1991) or "Controlled source tensor magnetotellurics" (Li and Pedersen, 1991).

In **Paper III**, CSEM impedance tensor and VMTF components defined as

$$\begin{aligned} Z_{xx} &= \frac{\tilde{E}_{x1}\tilde{H}_{y2} - \tilde{E}_{x2}\tilde{H}_{y1}}{\tilde{H}_{x1}\tilde{H}_{y2} - \tilde{H}_{x2}\tilde{H}_{y1}}, & Z_{xy} &= \frac{\tilde{E}_{x2}\tilde{H}_{x1} - \tilde{E}_{x1}\tilde{H}_{x2}}{\tilde{H}_{x1}\tilde{H}_{y2} - \tilde{H}_{x2}\tilde{H}_{y1}}, \\ Z_{yx} &= \frac{\tilde{E}_{y1}\tilde{H}_{y2} - \tilde{E}_{y2}\tilde{H}_{y1}}{\tilde{H}_{x1}\tilde{H}_{y2} - \tilde{H}_{x2}\tilde{H}_{y1}}, & Z_{yy} &= \frac{\tilde{E}_{y2}\tilde{H}_{x1} - \tilde{E}_{y1}\tilde{H}_{x2}}{\tilde{H}_{x1}\tilde{H}_{y2} - \tilde{H}_{x2}\tilde{H}_{y1}}, \\ T_x &= \frac{\tilde{H}_{z1}\tilde{H}_{y2} - \tilde{H}_{z2}\tilde{H}_{y1}}{\tilde{H}_{x1}\tilde{H}_{y2} - \tilde{H}_{x2}\tilde{H}_{y1}}, & T_y &= \frac{\tilde{H}_{z2}\tilde{H}_{x1} - \tilde{H}_{z1}\tilde{H}_{x2}}{\tilde{H}_{x1}\tilde{H}_{y2} - \tilde{H}_{x2}\tilde{H}_{y1}}. \end{aligned} \quad (2.9)$$

where \tilde{E}_{x1} , \tilde{E}_{y1} , \tilde{H}_{x1} , \tilde{H}_{y1} , \tilde{H}_{z1} and \tilde{E}_{x2} , \tilde{E}_{y2} , \tilde{H}_{x2} , \tilde{H}_{y2} , \tilde{H}_{z2} are the horizontal electric and magnetic field components aligned in x -, y - or z -direction. They are obtained with two independent source polarisations (subscripts 1 and 2).

Unlike in the plane-wave case, CSEM impedance tensor and VMTF components do not only depend on subsurface resistivities and frequencies but also on the positions of sources and receivers.

By investigating CSEM impedance tensor and VMTF components for electric and magnetic dipole/bipole sources in a homogeneous half space (Smirnova et al., 2023; Li and Pedersen, 1991), the following behaviour can be inferred for each zone:

- Near-field zone: For an electric source, the real part of the impedance tensor is constant and the imaginary part tends towards zero, i.e. the impedance tensor gets less dependent on the frequency towards the zero-frequency limit. For magnetic sources, real and imaginary parts of the impedance tensor tend towards zero. For both source types, the VMTF does not carry information about the resistivity in the DC limit.
- Transition zone: For both electric and magnetic sources, the impedance tensor and VMTF components are non-zero.
- Far-field zone: For both, electric and magnetic source types, the diagonal impedance tensor components (Z_{xx}, Z_{yy}) are zero and the absolute values of the real and imaginary off-diagonal components are nearly identical ($|Re(Z_{xy})| \approx |Im(Z_{xy})| \approx |Re(Z_{yx})| \approx |Im(Z_{yx})|$). T_x and T_y approach zero.

Impedance tensors and VMTF components can be used as input data for a CSEM inversion algorithm. A big advantage of using impedance tensors and VMTF compared to CSEM field components is that they are independent of the source current (Li and Pedersen, 1991), thus the current time series does not need to be recorded. However, evaluating CSEM field components might provide better resolution than using impedances (Smirnova et al., 2023; Sasaki et al., 2015). **Paper IV** compares both input data types, field components and impedance tensor & VMTF transfer functions, regarding their effects on the inversion result in 3D CSEM inversion.

2.4 3-D forward modelling

The term "electromagnetic forward modelling" (Fig. 2.5) describes the procedure of simulating electric and magnetic fields at a number of receiver locations for a known measurement setup and subsurface resistivity distribution (physical field problem). The first step in the forward modelling process is to formulate the appropriate mathematical model, also called boundary value problem (BVP), for the particular EM method of choice. For simple 1-D models, there exist analytic or semi-analytic solutions that solve this problem. For 2-D and 3-D models, the solution has to be approximated numerically, which requires a discrete formulation of the BVP. Thus, one has to decide on a suitable discretisation approach and subdivide the computational domain into small elements, so that accurate forward responses can be obtained. This process is called meshing. With the discrete equations and the information on the subsurface model and the measurement setting, a linear system of algebraic equations (SOE) is assembled and appropriate boundary conditions are applied. Afterwards, the system of equations is solved and the discrete solution is used to obtain the electric and magnetic fields at the locations of interest in the model domain. A 3-D EM forward modelling code consists of procedures for reading a particular 3-D model mesh and information, for assembling and solving a linear system of equations, and for computing forward responses, i.e. the EM fields at the receiver sites. The accuracy of the simulated fields can be assessed by comparing the forward responses to a reference solution or by estimating discretisation errors with an error estimation approach (cf. Sec. 2.4.3). To obtain more accurate results, the discretisation of the model domain can be improved, i.e. mesh refinement can be performed (Fig. 2.5).

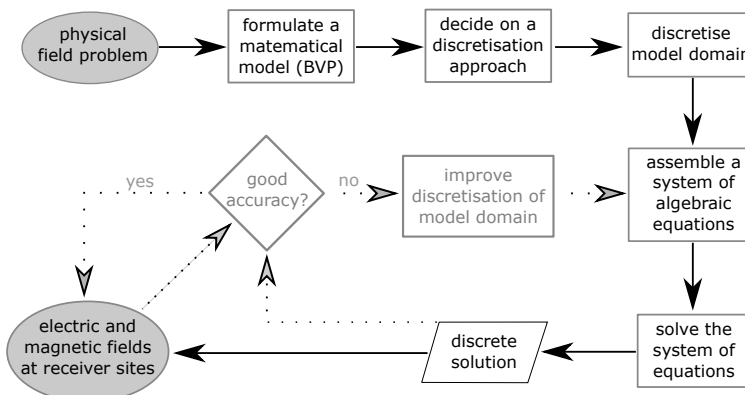


Figure 2.5. Procedure of an EM forward modelling process as implemented in `elife3D`. Black arrows illustrate the main paths of a forward modelling process. Dotted arrows represent paths that may be iterated if mesh refinement is applied.

2.4.1 Boundary value problem

The BVP for the EM field propagation in CSEM applications is a partial differential equation derived from Faraday's (eq. 2.1) and Ampère's (eq. 2.2) laws. In the modelling code introduced in **Paper I**, the so-called total electric field formulation is used, which is a second-order partial differential equation:

$$\begin{aligned} \nabla \times \frac{1}{\mu} \nabla \times \mathbf{E} + i\omega \frac{1}{\rho} \mathbf{E} - \omega^2 \varepsilon \mathbf{E} &= -i\omega \mathbf{J}_p \quad \text{in } \Omega, \\ \hat{\mathbf{n}} \times \mathbf{E} &= 0 \quad \text{on } \partial\Omega \end{aligned} \quad (2.10)$$

within the computational domain Ω . At the domain boundary, homogeneous Dirichlet boundary conditions are applied, assuming that the field has decayed to zero and ensuring the uniqueness of the electric field \mathbf{E} . Equation 2.10 is well-known as the "curl-curl equation" in terms of the electric field. To obtain solutions for two independent source orientations as required for CSEM tensor data, the equation has to be solved two times with the respective source terms \mathbf{J}_p . Model parameters in the forward modelling process are the material properties ρ , μ and ε (introduced in Section 2.1), which are spatially variable within the 3-D modelling domain, but approximated to be element-wise constant, isotropic and frequency-independent. The air region is also part of the modelling domain and is fixed to a resistivity of $10^8 \Omega\text{m}$.

Several numerical methods for computing approximate solutions for the BVP in two and three dimensions exist. In the forward modelling code presented in this thesis, the Finite Element Method (FEM) in combination with tetrahedral element shapes is used. This is common method to solve EM geophysical problems. Note, that the BVP and all subsequent equations are formulated with a time dependency of $e^{-i\omega t}$ in **Paper I**, whereas the implementation had to be changed to a time dependency of $e^{i\omega t}$ at a later stage (**Papers III & IV**) for compatibility reasons. Therefore, Maxwell's equations, the BVP and all depending equations are formulated in terms of the latter in this thesis.

2.4.2 Finite-element formulation

The strong formulation of the BVP (eq. 2.10) constitutes a continuous differential equation. For working with a numerical approximation method (such as the FEM) the weak formulation of the BVP has to be defined. It is relaxing the continuity and differentiability requirements of the strong formulation, but enables to solve the BVP numerically. Then, the fields within each element are approximated by a shape function, in this case a linear polynomial, with a finite number of degrees of freedom. This results in an approximate local description of the BVP by a set of equations. How to obtain the weak FE formulation of the BVP and its discrete formulation using the edge-based vector FE formulation is described in detail in Jin (2014) and in appendix A2 of **Paper I**. Accordingly, the discrete weak form of the curl-curl equation for the total electric field using first-order Nédélec vector FE on a tetrahedral mesh reads

$$\begin{aligned} \sum_{j=1}^6 E_j^e \iiint_{V^e} \frac{1}{\mu^e} (\nabla \times \mathbf{N}_l^e) \cdot (\nabla \times \mathbf{N}_j^e) dV - \sum_{j=1}^6 E_j^e \iint_{S^e} \frac{1}{\mu^e} (\mathbf{N}_l^e \times \nabla \times \mathbf{N}_j^e) \cdot \hat{n} dS \\ + \sum_{j=1}^6 E_j^e i\omega \iiint_{V^e} \left(\frac{1}{\rho^e} + i\omega \epsilon^e \right) \mathbf{N}_l^e \cdot \mathbf{N}_j^e dV \\ = -i\omega \iiint_{V^e} \mathbf{N}_l^e \cdot \mathbf{J}_p^e dV, \end{aligned} \quad (2.11)$$

defined for each element e of volume V^e and surface S^e in the modelling domain Ω using an $e^{i\omega t}$ time dependence. E_j^e denotes the unknown coefficient for the total electric field along the j th edge of element e . \mathbf{N}_l^e and \mathbf{N}_j^e define the first-order Nédélec basis functions using the element edge counters $l, j = 1, \dots, 6$. The surface integral term cancels along the inner domain boundaries due to the continuity of the electric field.

Equation 2.11 results in a local SOE for each element in the computational domain. All local SOE have to be assembled to a global SOE ($\mathbf{A}\mathbf{E} = \mathbf{b}$) comprising the physics of EM field propagation within the input subsurface model as well as the spatial relation of the elements to each other. This global system is solved for the electric field E_j along each edge j in the domain that is the vector \mathbf{E} . Therefore, for lowest order (linear) interpolation functions, the total number of edges in a discretised model determines the problem size, i.e. the number of degrees of freedom (DOF). Details on the global SOE assembly and the implementation of sources and receivers in the equations can be found in appendices A3 and A4 of **Paper I**.

2.4.3 Meshing and mesh refinement

To apply the FEM as mentioned above, the computational domain needs to be subdivided into small but finite-sized elements of tetrahedral shape (Fig. 2.6). The collection of all elements constitutes the so-called mesh. Each element consists of four nodes, six edges and four faces, which are shared with the neighbouring elements. The accuracy of the forward responses strongly depends on the mesh. The EM fields can be modelled more accurately on a mesh composed of a large number of small, high-quality elements compared to fields obtained on a coarse mesh with low-quality elements, i.e. extremely acute and flat inner angles of the tetrahedra. For CSEM applications, small elements at receiver sites and sources can substantially improve the solution accuracy (e.g. Puzyrev et al., 2013).

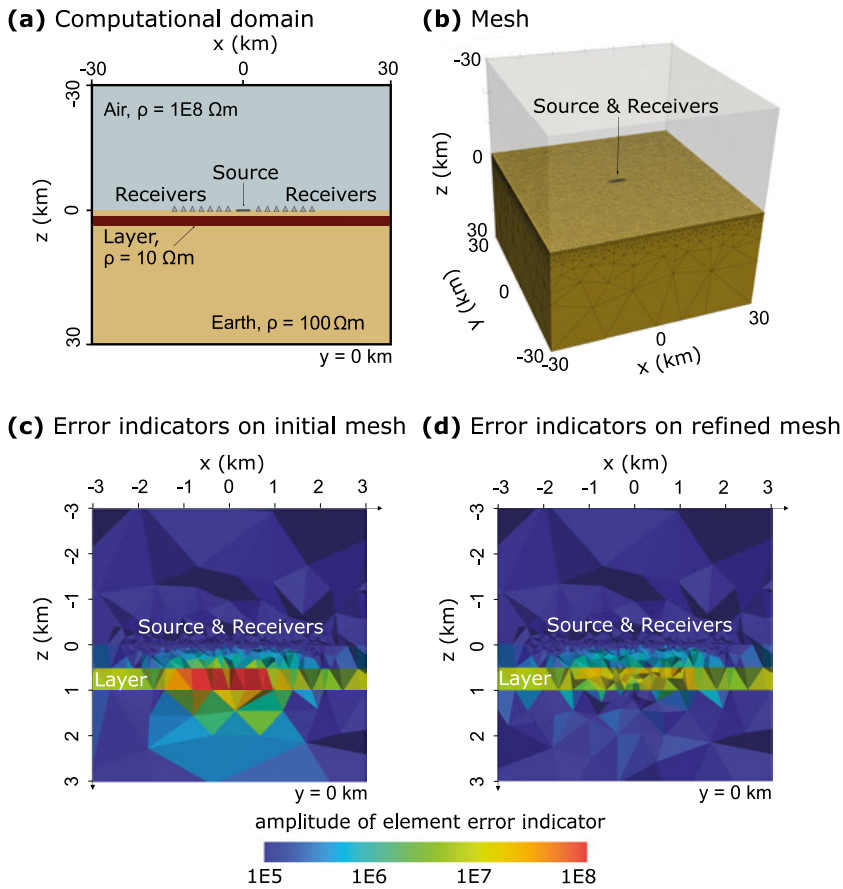


Figure 2.6. Illustration of meshing and mesh refinement performed with `elfe3D`: vertical cut through a 3-D computational domain of a layered model (a), 3-D view of the model with outer element edges of the lower half space illustrating the mesh (b), vertical cut and zoom into the modelling domain with element error indicators of an initial (c) and a refined (d) mesh.

It can be challenging to obtain accurate forward responses for complex models when using lowest order interpolation functions. To improve the modelling accuracy, the model domain can be either discretised globally very finely or the order of interpolation functions has to be increased (e.g. Castillo-Reyes et al., 2018; Rochlitz et al., 2019; Weiss et al., 2023a). Both approaches can result in large problem sizes and computational costs. Another option is to implement adaptive mesh refinement (Spitzer, 2023). To run such a mesh refinement, a coarse input mesh is designed manually and an automatic refinement procedure modifies the input mesh step-wise in areas which have to be discretised with smaller elements to achieve better solution accuracy at the receiver sites. A goal-oriented adaptive mesh refinement approach is implemented in the forward modelling code `elfe3D` presented in **Paper I**.

The FE solution of the BVP is a numerical approximation and is therefore affected by numerical modelling errors. Thus, the true analytic solution and the numerical approximation will always slightly deviate. As one cannot calculate the analytic solution for complex multi-dimensional models, the numerical error has to be estimated. Goal-oriented error estimation considers not only the global error in form of the residual but also emphasises the errors at the observation points, i.e. the receiver sites, within the model domain (e.g. Ren et al., 2013; Spitzer, 2023). To address the latter, an adjoint problem ($\mathbf{AW} = \mathbf{c}$) has to be set up and solved additionally to the primal boundary value problem. The main mathematical concepts that explain the requirement of an adjoint problem as applied in **Paper I**, are described in detail in Oden and Prudhomme (1999, 2001).

During an adaptive mesh refinement approach, error indicators, also called error estimators, are calculated for each element in the modelling domain (Fig. 2.6). Elements with the highest error estimators are identified and, in each refinement step, these elements are bisected, if they exceed a certain threshold. The definition of an adjoint problem specifically adapted to CSEM problems, the calculation of error estimators based on residuals and continuity conditions that are not already granted by the choice of shape functions as well as the refinement procedure are outlined in **Paper I**.

2.5 3-D inversion

The goal of collecting CSEM data is to investigate the electrical resistivity distribution of the subsurface below the receiver stations. In complex geological settings the subsurface resistivities cannot easily be determined from CSEM data. Therefore, a process called inversion has to be performed (e.g. Zhdanov, 2002). A geophysical inversion workflow aims at improving an initial guess of a subsurface model by minimising an average misfit measure between measured and forward modelled data. This is achieved by step-wise updating the initial model using an optimisation algorithm until a subsurface model is found that produces forward data fitting the observed data to an acceptable level. Due to computational resource limitations, EM data used to be evaluated with 1-D or 2-D inversion approaches. This is applicable in many marine environments with layered stratigraphy or land-based scenarios where a dominant geoelectrical strike direction can be determined. However, for more complex settings and higher-quality interpretations, 3-D inversion becomes important (Oldenburg et al., 2020) and nowadays technically possible.

As described in **Paper III**, an NLCG inversion algorithm previously incorporated in the in-house inversion software *emilia* by Zbinden (2015) for 2-D magnetotelluric inversion was further developed to enable 3-D CSEM inversion. The following two sections elaborate on the concepts of non-linear inversion theory in order to put the specific NLCG algorithm used and extended for this PhD thesis into context. Implementation details of the 3-D CSEM modules are provided in Section 3.2.

2.5.1 Non-linear inversion methods

Geophysical data inversion aims at finding a model \mathbf{m} producing simulated data $\mathbf{F}(\mathbf{m})$ that fit the observed data \mathbf{d}^{obs} within their uncertainty level u_n^2 (Menke, 2012). At the start of any inversion process, the inverse problem must be parametrised. The data vector \mathbf{d}^{obs} and the model vector \mathbf{m} holding free model parameters for specified elements in a discretised model domain have to be set. The decisions on data components and a-priori information to be included in an inversion depend on the user (cf. Section 2.3). Also, a suitable model discretisation (cf. Section 2.4.3) and start model have to be chosen. For non-linear inverse problems, the solution is dependent on the choice of the inverse algorithm and the related parametrisation (Menke, 2012). The EM inverse problem is a non-linear one, i.e. the model parameters are not linearly dependent on the observed or predicted data. Therefore, the model parametrisation has to be chosen carefully.

The objective function to be minimised in a non-linear inversion process is a weighted difference between measured and simulated data $\Phi_d(\mathbf{m})$. To stabilise this ill-posed problem (Zhdanov, 2009), a common approach is to add a regularisation term $\Phi_m(\mathbf{m})$ (e.g. Tikhonov and Arsenin, 1977) in order to make

the solution unique (Avdeev, 2005). The regularisation term aims at imposing some model characteristics, such as smooth or rough resistivity transitions. An objective function Φ for such an inverse problem can be formulated as

$$\begin{aligned}\Phi(\mathbf{m}) &= \Phi_d(\mathbf{m}) + \lambda \Phi_m(\mathbf{m}) \\ &= (\mathbf{d}^{obs} - \mathbf{F}(\mathbf{m}))^T \mathbf{C}_d^{-1} (\mathbf{d}^{obs} - \mathbf{F}(\mathbf{m})) \\ &\quad + \lambda (\mathbf{m} - \mathbf{m}_{ref})^T \mathbf{C}_m^{-1} (\mathbf{m} - \mathbf{m}_{ref}),\end{aligned}\tag{2.12}$$

where $\mathbf{C}_d = \text{diag}(u_n^2)$ is the data covariance matrix containing the data uncertainty u for each datum n . \mathbf{C}_m is the model regularisation matrix, \mathbf{m}_{ref} is an optional reference model and T is the transpose operator. The Lagrange multiplier λ controls the strength of the model regularisation.

The objective function has to be minimised with a numerical method. A possible strategy is to perform a global optimisation procedure, i.e. find a global minimum of the function with a grid-search method (Menke, 2012). A more efficient approach is to use a directed search technique, such as a gradient based method, that identifies a descent direction and applies a local linearisation of the objective function. Therefore, the non-linear inverse problem is step-wise linearised around the current model \mathbf{m}_k by Taylor series expansion (Menke, 2012)

$$\begin{aligned}\mathbf{F}(\mathbf{m}_{k+1}) &\approx \mathbf{F}(\mathbf{m}_k) + \left[\frac{\partial F_n(\mathbf{m})}{\partial m_i} \right]_{\mathbf{m}=\mathbf{m}_k} (\mathbf{m}_{k+1} - \mathbf{m}_k) \\ &= \mathbf{F}(\mathbf{m}_k) + \mathbf{J}(\mathbf{m}_{k+1} - \mathbf{m}_k),\end{aligned}\tag{2.13}$$

where the subscript k denotes the iteration number. Here, \mathbf{J} is the so-called sensitivity matrix or Jacobian that holds the partial derivatives of the n -th datum with respect to (w.r.t.) the i -th model parameter. $\mathbf{F}(\mathbf{m}_{k+1})$ is the predicted data vector of the updated model. When inserting equation 2.13 into equation 2.12, a modified objective function is produced that is quadratic in \mathbf{m}_{k+1} . The model \mathbf{m}_{k+1} that minimises this quadratic function can be obtained. Thus, by local linearisation of the non-linear inverse problem, a set of linear equations can be solved, in which the data vector is a linear function of the changes in the model parameters. This is only possible in the vicinity of the current model \mathbf{m}_k for small changes in the model parameters. Therefore, the non-linear inverse problem is solved in many small steps called iterations. Depending on the character of the specific inverse problem, the objective function may have several local minima in addition to a global minimum. It has to be mentioned that linearised constrained inversion applying directed search techniques is a deterministic inversion approach and thus dependent on the initial model \mathbf{m}_0 (Paasche and Tronicke, 2014). Therefore, such an inversion can be trapped more easily in local minima than global optimisation techniques.

2.5.2 Non-linear conjugate-gradient inversion

Several methods exist to solve non-linear inverse problems. Among them non-linear Newton-type iterations or the NLCG method are frequently applied to solve EM inverse problems (Avdeev, 2005). The convergence behaviour of, for instance, the Gauss-Newton method is superior to NLCG in terms of iterations. However, the single iterations are time consuming as the full Jacobian has to be obtained in each iteration. The NLCG method was adapted from the conjugate-gradient method to enable solving a non-linear inverse problem, i.e. minimising any continuous function for which the gradient can be computed (Fletcher and Reeves, 1964; Polak and Ribiere, 1969; Shewchuk, 1994). The very first EM algorithms using NLCG were reported by Rodi and Mackie (2001) for 2-D MT and Newman and Alumbaugh (2000) for 3-D MT inversion.

In each iteration of an NLCG inversion process, search directions are computed. The search directions, scaled by a step size, determine the direction and amount of changes in the model parameters. The updated model leads to predicted data that are more similar to the observed data than the predicted data of the previous iteration. An initial search direction is set to the steepest descent direction, i.e. the negative gradient of the objective function. Optimally, all subsequent search directions are conjugate directions (Shewchuk, 1994). However, the more the objective function deviates from a quadratic function, i.e. the more non-linear the inverse problem is, the easier the search directions can loose conjugacy. In addition to a possible presence of local minima in the objective function, this affects the convergence properties of NLCG (Shewchuk, 1994).

The important ingredient necessary to define the search directions at each iteration is the gradient of the objective function

$$\begin{aligned}\nabla\Phi(\mathbf{m}) &= \nabla\Phi_d(\mathbf{m}) + \lambda \nabla\Phi_m(\mathbf{m}) \\ &= -2\mathbf{J}^T \mathbf{C}_d^{-1}(\mathbf{d}^{obs} - \mathbf{F}(\mathbf{m})) + 2\lambda \mathbf{C}_m^{-1} \mathbf{m}.\end{aligned}\tag{2.14}$$

The gradients can be obtained without computing the sensitivity matrix \mathbf{J} explicitly (Rodi and Mackie, 2001; Newman and Alumbaugh, 2000), which is a big advantage of the NLCG method compared to other approaches. Therefore, a single NLCG iteration is comparably fast. The implemented NLCG algorithm is outlined in **Paper III**. Further implementation related details are provided in Section 3.2 of this thesis.

3. Implementation

A large fraction of the work reported on in this thesis comprised code development. Therefore, this chapter outlines the implementations of the developed 3-D forward and inverse modelling codes. The codes are written in modern Fortran using automatic vectorisation and shared-memory parallelisation (OpenMP). The forward modelling routines were designed from scratch, composed into a standalone code (`elfe3D`) and then implemented into the inversion framework `emilia` (Kalscheuer et al., 2008, 2010, 2015). External software libraries are linked, for instance to solve the systems of equations with PARDISO (Alappat et al., 2020; Bollhöfer et al., 2020, 2019) or MUMPS (Amestoy et al., 2001) and to generate tetrahedral meshes (Fig. 3.1) with `tetgen` (Si, 2015) in the adaptive refinement procedure. Furthermore, sparse matrix routines from the SPARSEKIT package (Saad, 1994) were modified and included.

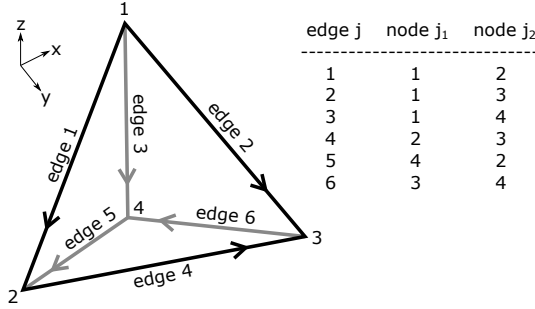


Figure 3.1. Tetrahedron with numbered nodes and edges as well as lookup table for local edge and node numbering scheme for the mesh elements. Node i_1 and node i_2 denote the start and end nodes of each edge, respectively. Modified after Jin (2014; pp. 263-264).

3.1 Forward modelling code

The 3-D CSEM forward modelling code `elfe3D` solves the two SOE ($\mathbf{A}\mathbf{E} = \mathbf{b}$, $\mathbf{A}\mathbf{W} = \mathbf{c}$) resulting from the edge-based vector FE formulation of the BVP (eq. 2.11) and the adjoint problem for error estimation (**Paper I**). The solution vector \mathbf{E} is then used to calculate the electric and magnetic field values $\tilde{\mathbf{E}}^e = (\tilde{E}_x, \tilde{E}_y, \tilde{E}_z)^T$ and $\tilde{\mathbf{H}}^e = (\tilde{H}_x, \tilde{H}_y, \tilde{H}_z)^T$ at the receiver stations in a model.

Before running the code, a text file containing model information has to be created. This includes the locations and numbers of receivers and sources, the source type, the frequencies, the refinement parameters and the mesh file names. Furthermore, a tetrahedral FE mesh has to be generated using the open-source mesh generator *tetgen* (Si, 2015). For complex models, *FacetModeller* (Lelièvre et al., 2018) can be utilised to construct a 3-D mesh out of 2-D model slices. The final input file for the mesh generator has to be set up manually without a graphical user interface. The mesh and models can be viewed as *.vtk*-files in *paraview* (Ahrens et al., 2005). The structure of the 3-D CSEM forward modelling code is outlined in Algorithm 1. In the following, implementation details of the code routines are explained.

Algorithm 1 3-D CSEM forward modelling with mesh refinement in *elfe3D*

```

read model and refinement information
if (Nfreq > 1 .and. Nrefsteps > 0 )
    write error message: 'Refinement only possible for a single frequency'
    termination_criterion  $\leftarrow$  1
else
    termination_criterion  $\leftarrow$  0
    refinement_step  $\leftarrow$  0
end if
while termination_criterion == 0 do
    Routine I: read mesh files
    Routine II: assemble connectivity matrices
    Routine III: obtain model properties
    Routine IV: calculate linear interpolation functions
    do numfreq = 1, Nfreq
        Routine V: assemble global system matrix A in sparse COO format
        Routine VI: calculate global RHS for primal and adjoint BVP
        Routine VII: apply boundary conditions
        Routine VIII: optional conversion of matrix A to CSR format
        Routine IX: apply direct solver to solve primal and adjoint BVP
        Routine X: error estimation
        if (mesh requirements are met) termination_criterion  $\leftarrow$  1
        if (termination_criterion == 0)
            generate refined mesh
            refinement_step  $\leftarrow$  refinement_step + 1
        else if (termination_criterion == 1)
            calculate E- and H-field responses at receivers
        end if
    end do
end while

```

The program (Algorithm 1) starts with reading the model and refinement information. Forward modelling without mesh refinement can be performed for multiple frequencies ($Nfreq > 1$). Mesh refinement ($Nrefsteps > 0$) can only be performed for a single frequency, as a refined mesh is frequency-specific (cf. **Paper I**). If the input parameters $Nfreq$ and $Nrefsteps$ do not contradict each other, the termination criterion and refinement step are initialised to zero. Afterwards, an outer refinement loop is started. This loop over the forward modelling procedure includes the generation of a new, refined mesh at each refinement step, if the mesh requirements are not met. The loop termination criterion is set to 1, if one of the predefined mesh requirements is met (such as the maximum number of refinement steps $Nrefsteps$, the maximum allowed problem size, the accuracy tolerance). This means that all subsequent routines are repeated until one mesh criterion is met. If the number of refinement steps is zero ($Nrefsteps = 0$), only forward modelling on the input mesh is performed.

Routine I: read mesh files

The following mesh files produced by the mesh generator `tetgen` are read: `xxx.edge`, `xxx.node`, `xxx.ele`, `xxx.face`, `xxx.neigh` and `xxx.vtk` (Si, 2020). The `vtk`-file must contain the model parameters, i.e. ρ , ε and μ for each model cell. The mesh information is saved in arrays as indicated in Table 3.1 for the node coordinate array.

Table 3.1. Array containing Cartesian coordinates (x,y,z) of all nodes of the mesh. N : total number of nodes.

N x 3	x	y	z
node 1			
node 2			
...			
node N			

Routine II: assemble connectivity matrices

The relation between global element numbers and global edge numbers is essential for assembling the global system of equations in Routines V and VI. Therefore, an element to edge number array (Table 3.2) is constructed after a specified edge to node connection scheme for elements (cf. Fig. 3.1).

In an unstructured mesh, the uniqueness of the mesh has to be ensured by specifying directions to all edges (i.e. DOF) to account for possible differences in local and global edge directions. Therefore, an *edge_sign* array of size $[M \times 6]$ is constructed and the corresponding entries must be included in every calculation that involves the edge-based Nédélec vector shape functions. The *edge_sign* array is calculated as follows using an *element2node* array that

Table 3.2. The array *elements2edges* relates global element numbers to global edge numbers. *M*: total number of elements.

M x 6	edge 1	edge 2	edge 3	edge 4	edge 5	edge 6
element 1						
element 2						
...						
element M						

connects each element with its four node numbers and taking the connectivity scheme for nodes and elements (Fig. 3.1) into account:

```

1  ed_sign(:,1) = element2node(:,1) - element2node(:,2)
2  ed_sign(:,1) = ed_sign(:,1)/abs(ed_sign(:,1))
3  ed_sign(:,2) = element2node(:,1) - element2node(:,3)
4  ed_sign(:,2) = ed_sign(:,2)/abs(ed_sign(:,2))
5  ed_sign(:,3) = element2node(:,1) - element2node(:,4)
6  ed_sign(:,3) = ed_sign(:,3)/abs(ed_sign(:,3))
7  ed_sign(:,4) = element2node(:,2) - element2node(:,3)
8  ed_sign(:,4) = ed_sign(:,4)/abs(ed_sign(:,4))
9  ed_sign(:,5) = element2node(:,4) - element2node(:,2)
10 ed_sign(:,5) = ed_sign(:,5)/abs(ed_sign(:,5))
11 ed_sign(:,6) = element2node(:,3) - element2node(:,4)
12 ed_sign(:,6) = ed_sign(:,6)/abs(ed_sign(:,6))

```

Routine III: obtain model properties

Essential model properties are obtained though combining model and mesh information. Arrays with element volumes V^e , edge lengths h_j , element resistivities ρ^e , element magnetic permeabilities μ^e and element dielectric permittivities ε^e are constructed. Furthermore, source edges, boundary edges and PEC edges are determined. Electric and magnetic sources are modelled via line or loop sources along element edges. The sources are constructed of straight source segments included in the mesh at the specific source locations. Elements containing the receiver sites are identified.

Afterwards, an inner loop over all chosen frequencies f is started, which is only iterated if no refinement is performed. The frequency loop is an inner loop, as Routine I-IV do only perform computations that are frequency-independent.

Routine IV: calculate linear interpolation functions

With the mesh information, an unknown function Ψ can be linearly approximated within each element e by

$$\Psi^e(x, y, z) = a^e + b^e x + c^e y + d^e z. \quad (3.1)$$

Arrays for the linear interpolation function coefficients a , b , c and d are computed for each edge from the mesh coordinates using an expansion of determinants (Jin, 2014; pp. 153-155). Linear interpolation functions can then be obtained by

$$L_j^e(x, y, z) = \frac{1}{6V^e} (a_j^e + b_j^e x + c_j^e y + d_j^e z). \quad (3.2)$$

Using the linear interpolation functions $L_{j\text{start}}$ and $L_{j\text{end}}$ of two adjacent nodes along an edge and the edge lengths, edge-based vector (Nédélec) shape functions can be calculated (Jin, 2014; pp. 263-264). This is performed without storing extra arrays as

$$\mathbf{N}_j^e = (L_{j\text{start}} \nabla L_{j\text{end}} - L_{j\text{end}} \nabla L_{j\text{start}}) h_j. \quad (3.3)$$

Routine V: assemble global system matrix \mathbf{A} in sparse COO format

The local system matrix for each element results from the edge-based FE formulation (eq. 2.11) and the equation for interpolating the approximated electric fields at the edges of an element E_j^e to the E-field components $\tilde{\mathbf{E}}^e = (\tilde{E}_x, \tilde{E}_y, \tilde{E}_z)^T$ at a discrete point in the element as

$$\tilde{\mathbf{E}}^e = \sum_{j=1}^6 \mathbf{N}_j^e E_j^e. \quad (3.4)$$

Then, the local system matrix reads

$$A_{lj}^e = K_{lj}^e + i\omega \left(\frac{1}{\rho^e} + i\omega \varepsilon^e \right) M_{lj}^e, \quad l, j = 1, \dots, 6, \quad (3.5)$$

where $K_{lj}^e = \iiint_{V^e} \frac{1}{\mu^e} (\nabla \times \mathbf{N}_l^e) \cdot (\nabla \times \mathbf{N}_j^e) dV$ and $M_{lj}^e = \iiint_{V^e} \mathbf{N}_l^e \cdot \mathbf{N}_j^e dV$. The local matrices are calculated using the linear interpolation function coefficient arrays from Routine III (Jin, 2014; pp. 268-269) in a loop over all mesh elements. Local matrices are not stored, but directly assembled to the global complex system matrix \mathbf{A} in sparse coordinate (COO) format.

If the forward routines are called within the NLCG inversion algorithm (cf. Sec. 3.2), derivatives of the local system matrices w.r.t. transformed inversion model parameters $\frac{\partial \mathbf{A}^e}{\partial m_i}$ are required. This involves computation of

$$\frac{\partial A_{lj}^e}{\partial \rho^e} = \frac{\partial}{\partial \rho^e} \left(i\omega \frac{1}{\rho^e} M_{lj}^e \right) = -i\omega \frac{1}{(\rho^e)^2} M_{lj}^e \quad (3.6)$$

in this routine, which are stored in sparse COO format. Model parameter transformation (cf. **Paper III**) is accounted for in the gradient computation routines (Sec. 3.2.1).

Routine VI: calculate global RHS for primal and adjoint BVP

The source terms, or right-hand side (RHS) vectors \mathbf{b} and \mathbf{c} , of the primal and adjoint problems are set up. The element source term of the primal BVP is given by

$$b_l^e = -i\omega \iiint_{V^e} \mathbf{N}_l^e \cdot \mathbf{J}_p^e dV \quad \text{with } l = 1, \dots, 6. \quad (3.7)$$

With information on the global source edge numbers, the global primal RHS \mathbf{b} for the current angular frequency ω and a defined source current term \mathbf{J}_p^e is directly obtained. The source contributions to the adjoint source term are located at the receiver sites. The source strengths in the adjoint problem take the distance of each adjoint source to the primal source into account (cf. **Paper I**). In a loop over all receiver sites, the local adjoint source terms are calculated and directly assembled to the global adjoint RHS vector \mathbf{c} .

Routine VII: apply boundary conditions

Dirichlet boundary conditions (BC, eq. 2.10) are applied in two subroutines. The first subroutine sets the BC for the model domain boundary $\partial\Omega$. The second subroutine sets the same type of BC on edges within the modelling domain, where the electric field is supposed to be zero, i.e. PEC edges. With the latter, highly conductive materials in the model domain can be approximated (cf. **Paper II**). The BC are applied by setting the complex elements of the global system matrix \mathbf{A} that correspond to the boundary edges to (1.0, 0.0) and (0.0, 0.0) for the diagonal and non-diagonal elements of the system matrix, respectively.

Routine VIII: optional conversion of matrix A to CSR format

If direct solver PARDISO (Alappat et al., 2020; Bollhöfer et al., 2019, 2020) is used to solve the SOE in Routine IX, the system matrix needs to be stored in upper triangular complex sparse row (CSR) format. The conversion from COO to CSR format is optionally performed in this routine.

Routine IX: applying direct solver to solve primal and adjoint BVPs

Two direct solvers are implemented to solve the SOE: PARDISO (Alappat et al., 2020; Bollhöfer et al., 2020, 2019) and MUMPS (Amestoy et al., 2001). Their performance behaviour is very similar, but only MUMPS is currently freely available for the academic community. The calls to the solver routines include global system matrix analyses and checks, matrix factorisation and the final solve. The SOE of the primal and adjoint problems are solved in a single run, since the solver can handle multiple RHS. The advantage here is that the system matrix is the same for both, primal and adjoint problems. Thus, the time and memory demanding process of matrix factorisation has to be performed only once. In the forward modelling routines implemented in *emilia*, the solving is performed for not only one but two source polarisations, so that impedance tensor components can be obtained (cf. Sec. 2.3). Outputs of the

routine are the solution vectors \mathbf{E} and \mathbf{W} of the primal and adjoint problems, respectively.

Routine X: error estimation

Error estimation and new mesh generation is performed for the goal-oriented adaptive refinement option that can be combined with general mesh quality improvement. The goal-oriented refinement is based on error estimators for primal and an adjoint problems, similar to those presented by Ren et al. (2013) for 3-D MT modelling. The error estimators consist of three components: residuals, face jumps in the normal current density and face jumps in the tangential magnetic field (cf. **Paper I**), which are computed for each element within the mesh. Which of the components are to be included in the error estimation is customisable and can be defined by the user. The CSEM refinement has some special features, which are for instance that i) face jumps in tangential magnetic fields can be included in the error estimator, which is helpful for models with magnetic permeability contrasts, ii) a refinement option that allows to increase the mesh quality during the refinement or only in the last refinement step, which saves time and memory, iii) the use of an average relative global error estimator and an average relative error estimator at the receivers to assess the refinement behaviour. Furthermore, it was noticed that error estimation for goal-oriented refinement cannot be conducted in the same way as in MT, because the error estimation is dependent on the primal and the adjoint source terms. The source terms differ between MT and CSEM modelling. Therefore, the expression for the adjoint source ensures that all receiver locations are included equally in the error estimation. Additionally, the element error estimators are divided by the local field strengths avoiding amplitude-dependent over-refining of the mesh.

Utilising the element error estimators, the mesh can be refined at the necessary locations with a call to the mesh generator `tetgen`. If the termination criterion stops the loop, electric field responses are obtained via Equation 3.4. Magnetic field responses are obtained via Faraday's law as

$$\tilde{\mathbf{H}}^e = -\frac{1}{i\omega\mu} \sum_{j=1}^6 \nabla \times \mathbf{N}_j^e E_j^e. \quad (3.8)$$

In `emilia`, also impedance tensors and VMTF are calculated and saved in output files.

3.2 Inversion code

The inversion framework *emilia* (**E**lectromagnetic **I**nversion with **L**east **I**ntricate **A**lgorithms, Kalscheuer et al., 2008, 2010, 2015) is extended with new 3-D CSEM modules in this PhD project. In more detail, new abstract objects (Fig. 3.2) for i) CSEM field data, ii) 3-D CSEM forward and sensitivity computations, iii) 3-D tetrahedral models and iv) tetrahedral model regularisation are designed. Furthermore, the NLCG inversion algorithm implemented by Zbinden (2015) is adapted to handling large sparse regularisation matrices required for 3-D models. A general description of the 3-D CSEM NLCG inversion algorithm and examples of its application can be found in **Paper III**. The input data types are discussed in **Paper IV**. A complete list of input parameters for the preconditioned NLCG inversion algorithm is included in Zbinden (2015). The 3-D CSEM inversion code inverts for cell-wise constant electrical resistivities within an inner subset of the forward modelling mesh. In the following, I enlarge upon additional crucial details of the code implementation that did not find space in the above mentioned papers, but are of interest to draw a complete picture of the inversion related implementations of this work.

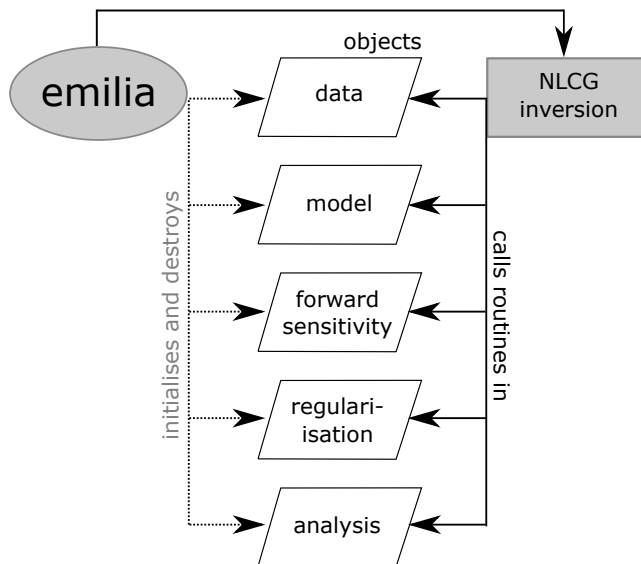


Figure 3.2. Simplified call-graph of the NLCG inversion procedure implemented in *emilia*. The main program *emilia* initialises and destroys the data, model, forward and sensitivity, regularisation and analysis objects. It also calls the inversion routine, that itself calls subroutines in the specific objects. Information passing is only possible through initialised class-variables and stays local within the objects otherwise.

3.2.1 Computation of data gradients

Data gradients $\nabla\Phi_d$ (eq. 2.14) have to be computed during the NLCG inversion (cf. **Paper III**). The full sensitivity matrix \mathbf{J} connecting changes in a proposed model to changes in the forward modelled data is expensive to obtain. Therefore, $\nabla\Phi_d$ is computed without explicit calculation of the Jacobian (e.g. Newman and Alumbaugh, 2000). It follows the derivation of the equations necessary to implement for $\nabla\Phi_d$ computation in terms of EM field components (**Paper IV**) as well as of impedance tensors and VMTF (**Paper III**).

As the governing BVP (eq. 2.10) is solved for the total electric field \mathbf{E} at the element edges j , the edge contribution to each EM field component at a station can be expressed by:

$$\begin{aligned} \tilde{E}_{xj} &= {}^e\boldsymbol{\eta}_{j(x)}^T \mathbf{E}, & \tilde{E}_{yj} &= {}^e\boldsymbol{\eta}_{j(y)}^T \mathbf{E}, & \tilde{E}_{zj} &= {}^e\boldsymbol{\eta}_{j(z)}^T \mathbf{E}, \\ \tilde{H}_{xj} &= {}^h\boldsymbol{\eta}_{j(x)}^T \mathbf{E}, & \tilde{H}_{yj} &= {}^h\boldsymbol{\eta}_{j(y)}^T \mathbf{E}, & \tilde{H}_{zj} &= {}^h\boldsymbol{\eta}_{j(z)}^T \mathbf{E}. \end{aligned} \quad (3.9)$$

The vector $\boldsymbol{\eta}$ is the *interpolation function*. $\boldsymbol{\eta}$ is defined using Nédélec shape functions \mathbf{N}_j^e (eq. 3.3). ${}^e\boldsymbol{\eta}_j = \mathbf{N}_j^e$ is the interpolation vector for the electric field components and ${}^h\boldsymbol{\eta}_j = -(i\omega\mu)^{-1}\nabla \times \mathbf{N}_j^e$ is the interpolation vector for the magnetic field components expressed in Cartesian coordinate directions $\boldsymbol{\eta}_{j(x)}$, $\boldsymbol{\eta}_{j(y)}$ and $\boldsymbol{\eta}_{j(z)}$. The derivatives of the fields w.r.t. the model parameters m_i can be computed as

$$\begin{aligned} \frac{\partial \tilde{E}_x}{\partial m_i} &= {}^e\boldsymbol{\eta}_{j(x)}^T \frac{\partial \mathbf{E}}{\partial m_i}, & \frac{\partial \tilde{E}_y}{\partial m_i} &= {}^e\boldsymbol{\eta}_{j(y)}^T \frac{\partial \mathbf{E}}{\partial m_i}, & \frac{\partial \tilde{E}_z}{\partial m_i} &= {}^e\boldsymbol{\eta}_{j(z)}^T \frac{\partial \mathbf{E}}{\partial m_i}, \\ \frac{\partial \tilde{H}_x}{\partial m_i} &= {}^h\boldsymbol{\eta}_{j(x)}^T \frac{\partial \mathbf{E}}{\partial m_i}, & \frac{\partial \tilde{H}_y}{\partial m_i} &= {}^h\boldsymbol{\eta}_{j(y)}^T \frac{\partial \mathbf{E}}{\partial m_i}, & \frac{\partial \tilde{H}_z}{\partial m_i} &= {}^h\boldsymbol{\eta}_{j(z)}^T \frac{\partial \mathbf{E}}{\partial m_i}. \end{aligned} \quad (3.10)$$

Since $\boldsymbol{\eta}$ is not dependent on the model parameters, only the partial derivatives of \mathbf{E} have to be determined. $\frac{\partial \mathbf{E}}{\partial m_i}$ can be obtained starting at the main SOE:

$$\begin{aligned} \mathbf{A}\mathbf{E} &= \mathbf{b} & \left| \frac{\partial(\cdot)}{\partial m_i} \right. \\ \frac{\partial}{\partial m_i}(\mathbf{A}\mathbf{E}) &= \frac{\partial \mathbf{b}}{\partial m_i} & \left| \frac{\partial \mathbf{b}}{\partial m_i} = 0 \right. \\ \frac{\partial \mathbf{A}}{\partial m_i}\mathbf{E} + \mathbf{A} \frac{\partial \mathbf{E}}{\partial m_i} &= 0 & \left| \Leftrightarrow \right. \\ \mathbf{A} \frac{\partial \mathbf{E}}{\partial m_i} &= -\frac{\partial \mathbf{A}}{\partial m_i}\mathbf{E} & \left| \mathbf{A}^{-1}(\cdot) \right. \\ \frac{\partial \mathbf{E}}{\partial m_i} &= -\mathbf{A}^{-1} \frac{\partial \mathbf{A}}{\partial m_i}\mathbf{E}. & \end{aligned} \quad (3.11)$$

Note, that in CSEM modelling with Dirichlet boundary conditions, $\frac{\partial \mathbf{b}}{\partial m_i} = 0$ holds as the source contributions (eq. 3.7) are independent of the modelling parameters m_i . Inserting Equation 3.11 into Equation 3.10, the expressions for the field derivatives are

$$\begin{aligned}\frac{\partial \tilde{E}_x}{\partial m_i} &= -^e \boldsymbol{\eta}_{j(x)}^T \mathbf{A}^{-1} \left(\frac{\partial \mathbf{A}}{\partial m_i} \mathbf{E} \right), & \frac{\partial \tilde{E}_y}{\partial m_i} &= -^e \boldsymbol{\eta}_{j(y)}^T \mathbf{A}^{-1} \left(\frac{\partial \mathbf{A}}{\partial m_i} \mathbf{E} \right), \\ \frac{\partial \tilde{E}_z}{\partial m_i} &= -^e \boldsymbol{\eta}_{j(z)}^T \mathbf{A}^{-1} \left(\frac{\partial \mathbf{A}}{\partial m_i} \mathbf{E} \right), \\ \frac{\partial \tilde{H}_x}{\partial m_i} &= -^h \boldsymbol{\eta}_{j(x)}^T \mathbf{A}^{-1} \left(\frac{\partial \mathbf{A}}{\partial m_i} \mathbf{E} \right), & \frac{\partial \tilde{H}_y}{\partial m_i} &= -^h \boldsymbol{\eta}_{j(y)}^T \mathbf{A}^{-1} \left(\frac{\partial \mathbf{A}}{\partial m_i} \mathbf{E} \right), \\ \frac{\partial \tilde{H}_z}{\partial m_i} &= -^h \boldsymbol{\eta}_{j(z)}^T \mathbf{A}^{-1} \left(\frac{\partial \mathbf{A}}{\partial m_i} \mathbf{E} \right).\end{aligned}\tag{3.12}$$

If electric and magnetic field components are input data for the inversion, the data gradients $\nabla \Phi_d$ are obtained via

$$\nabla \Phi_d(\mathbf{m}) = \frac{\partial \Phi_d}{\partial m_i} = -2Re \left[- \sum_{n=1}^N (\Delta d_n)^* \boldsymbol{\eta}_n^T \mathbf{A}^{-1} \left(\frac{\partial \mathbf{A}}{\partial m_i} \mathbf{E} \right) \right], \tag{3.13}$$

where $(\Delta d_n)^*$ is the complex-conjugate of the weighted data difference $\Delta d_n = (d_n^{obs} - F_n(\mathbf{m})) / u_n^2$ formulated in terms of the EM fields for each datum n . $\boldsymbol{\eta}_n^T$ is set by selecting the correct component from Equation 3.12 that is currently summed.

Defining

$$\mathbf{g}^T = -2 \sum_{n=1}^N (\Delta d_n)^* \boldsymbol{\eta}_n^T \tag{3.14}$$

and

$$\mathbf{v}^T = \mathbf{g}^T \mathbf{A}^{-1} \tag{3.15}$$

a pseudo-forward problem

$$\mathbf{A} \mathbf{v} = \mathbf{g} \tag{3.16}$$

can be solved to compute the first part of Equation 3.13 (Newman and Alumbaugh, 2000). The derivatives of the system matrix $\frac{\partial \mathbf{A}}{\partial m_i}$ are inexpensive to obtain and the computations are performed already in the forward modelling routine, when constructing the system matrix (Routine V in Sec. 3.1). The remaining operations to compute $\nabla \Phi_d$ are a single matrix-vector multiplication and a single vector-vector multiplication (eq. 3.13).

For impedance tensor and VMTF (eq. 2.9) input data, the $\nabla \Phi_d$ computations are more advanced. The impedance derivative equations were introduced by Newman and Alumbaugh (2000). The VMTF derivatives are calculated accordingly in this work. The following expressions constitute the impedance

(eq. 3.17) and VMTF (eq. 3.18) data derivatives w.r.t. the model parameters m_i :

$$\begin{aligned}
\frac{\partial Z_{xx}}{\partial m_i} &= C^{-2} \left[C \left(\tilde{H}_{y2} \frac{\partial \tilde{E}_{x1}}{\partial m_i} + \tilde{E}_{x1} \frac{\partial \tilde{H}_{y2}}{\partial m_i} - \tilde{H}_{y1} \frac{\partial \tilde{E}_{x2}}{\partial m_i} - \tilde{E}_{x2} \frac{\partial \tilde{H}_{y1}}{\partial m_i} \right) \right. \\
&\quad \left. - (\tilde{E}_{x1} \tilde{H}_{y2} - \tilde{E}_{x2} \tilde{H}_{y1}) \times \left(\tilde{H}_{y2} \frac{\partial \tilde{H}_{x1}}{\partial m_i} + \tilde{H}_{x1} \frac{\partial \tilde{H}_{y2}}{\partial m_i} - \tilde{H}_{y1} \frac{\partial \tilde{H}_{x2}}{\partial m_i} - \tilde{H}_{x2} \frac{\partial \tilde{H}_{y1}}{\partial m_i} \right) \right] \\
\frac{\partial Z_{xy}}{\partial m_i} &= C^{-2} \left[C \left(\tilde{H}_{x1} \frac{\partial \tilde{E}_{x2}}{\partial m_i} + \tilde{E}_{x2} \frac{\partial \tilde{H}_{x1}}{\partial m_i} - \tilde{H}_{x2} \frac{\partial \tilde{E}_{x1}}{\partial m_i} - \tilde{E}_{x1} \frac{\partial \tilde{H}_{x2}}{\partial m_i} \right) \right. \\
&\quad \left. - (\tilde{E}_{x2} \tilde{H}_{x1} - \tilde{E}_{x1} \tilde{H}_{x2}) \times \left(\tilde{H}_{y2} \frac{\partial \tilde{H}_{x1}}{\partial m_i} + \tilde{H}_{x1} \frac{\partial \tilde{H}_{y2}}{\partial m_i} - \tilde{H}_{y1} \frac{\partial \tilde{H}_{x2}}{\partial m_i} - \tilde{H}_{x2} \frac{\partial \tilde{H}_{y1}}{\partial m_i} \right) \right] \\
\frac{\partial Z_{yx}}{\partial m_i} &= C^{-2} \left[C \left(\tilde{H}_{y2} \frac{\partial \tilde{E}_{y1}}{\partial m_i} + \tilde{E}_{y1} \frac{\partial \tilde{H}_{y2}}{\partial m_i} - \tilde{H}_{y1} \frac{\partial \tilde{E}_{y2}}{\partial m_i} - \tilde{E}_{y2} \frac{\partial \tilde{H}_{y1}}{\partial m_i} \right) \right. \\
&\quad \left. - (\tilde{E}_{y1} \tilde{H}_{y2} - \tilde{E}_{y2} \tilde{H}_{y1}) \times \left(\tilde{H}_{y2} \frac{\partial \tilde{H}_{x1}}{\partial m_i} + \tilde{H}_{x1} \frac{\partial \tilde{H}_{y2}}{\partial m_i} - \tilde{H}_{y1} \frac{\partial \tilde{H}_{x2}}{\partial m_i} - \tilde{H}_{x2} \frac{\partial \tilde{H}_{y1}}{\partial m_i} \right) \right] \\
\frac{\partial Z_{yy}}{\partial m_i} &= C^{-2} \left[C \left(\tilde{H}_{x1} \frac{\partial \tilde{E}_{y2}}{\partial m_i} + \tilde{E}_{y2} \frac{\partial \tilde{H}_{x1}}{\partial m_i} - \tilde{H}_{x2} \frac{\partial \tilde{E}_{y1}}{\partial m_i} - \tilde{E}_{y1} \frac{\partial \tilde{H}_{x2}}{\partial m_i} \right) \right. \\
&\quad \left. - (\tilde{E}_{y2} \tilde{H}_{x1} - \tilde{E}_{y1} \tilde{H}_{x2}) \times \left(\tilde{H}_{y2} \frac{\partial \tilde{H}_{x1}}{\partial m_i} + \tilde{H}_{x1} \frac{\partial \tilde{H}_{y2}}{\partial m_i} - \tilde{H}_{y1} \frac{\partial \tilde{H}_{x2}}{\partial m_i} - \tilde{H}_{x2} \frac{\partial \tilde{H}_{y1}}{\partial m_i} \right) \right]
\end{aligned} \tag{3.17}$$

and

$$\begin{aligned}
\frac{\partial T_x}{\partial m_i} &= C^{-2} \left[C \left(\tilde{H}_{y2} \frac{\partial \tilde{H}_{z1}}{\partial m_i} + \tilde{H}_{z1} \frac{\partial \tilde{H}_{y2}}{\partial m_i} - \tilde{H}_{y1} \frac{\partial \tilde{H}_{z2}}{\partial m_i} - \tilde{H}_{z2} \frac{\partial \tilde{H}_{y1}}{\partial m_i} \right) \right. \\
&\quad \left. - (\tilde{H}_{z1} \tilde{H}_{y2} - \tilde{H}_{z2} \tilde{H}_{y1}) \times \left(\tilde{H}_{y2} \frac{\partial \tilde{H}_{x1}}{\partial m_i} + \tilde{H}_{x1} \frac{\partial \tilde{H}_{y2}}{\partial m_i} - \tilde{H}_{y1} \frac{\partial \tilde{H}_{x2}}{\partial m_i} - \tilde{H}_{x2} \frac{\partial \tilde{H}_{y1}}{\partial m_i} \right) \right] \\
\frac{\partial T_y}{\partial m_i} &= C^{-2} \left[C \left(\tilde{H}_{x1} \frac{\partial \tilde{H}_{z2}}{\partial m_i} + \tilde{H}_{z2} \frac{\partial \tilde{H}_{x1}}{\partial m_i} - \tilde{H}_{x2} \frac{\partial \tilde{H}_{z1}}{\partial m_i} - \tilde{H}_{z1} \frac{\partial \tilde{H}_{x2}}{\partial m_i} \right) \right. \\
&\quad \left. - (\tilde{H}_{z2} \tilde{H}_{x1} - \tilde{H}_{z1} \tilde{H}_{x2}) \times \left(\tilde{H}_{y2} \frac{\partial \tilde{H}_{x1}}{\partial m_i} + \tilde{H}_{x1} \frac{\partial \tilde{H}_{y2}}{\partial m_i} - \tilde{H}_{y1} \frac{\partial \tilde{H}_{x2}}{\partial m_i} - \tilde{H}_{x2} \frac{\partial \tilde{H}_{y1}}{\partial m_i} \right) \right]
\end{aligned} \tag{3.18}$$

with $C = (\tilde{H}_{x1} \tilde{H}_{y2} - \tilde{H}_{x2} \tilde{H}_{y1})$. These expressions contain only EM field components and their derivatives w.r.t. the model parameters. In the following, the total electric field solution \mathbf{E} is denoted as \mathbf{E}_1 or \mathbf{E}_2 , corresponding to two independent forward solutions, i.e. the two source polarisations required to

construct the impedance tensor and VMTF components. With Equation 3.12, field derivatives can be replaced:

$$\begin{aligned}
\frac{\partial Z_{xx}}{\partial m_i} &= -{}^1\boldsymbol{\gamma}_{j\ xx}^T \mathbf{A}^{-1} \left(\frac{\partial \mathbf{A}}{\partial m_i} \mathbf{E}_1 \right) - {}^2\boldsymbol{\gamma}_{j\ xx}^T \mathbf{A}^{-1} \left(\frac{\partial \mathbf{A}}{\partial m_i} \mathbf{E}_2 \right) \\
\frac{\partial Z_{xy}}{\partial m_i} &= -{}^1\boldsymbol{\gamma}_{j\ xy}^T \mathbf{A}^{-1} \left(\frac{\partial \mathbf{A}}{\partial m_i} \mathbf{E}_1 \right) - {}^2\boldsymbol{\gamma}_{j\ xy}^T \mathbf{A}^{-1} \left(\frac{\partial \mathbf{A}}{\partial m_i} \mathbf{E}_2 \right) \\
\frac{\partial Z_{yx}}{\partial m_i} &= -{}^1\boldsymbol{\gamma}_{j\ yx}^T \mathbf{A}^{-1} \left(\frac{\partial \mathbf{A}}{\partial m_i} \mathbf{E}_1 \right) - {}^2\boldsymbol{\gamma}_{j\ yx}^T \mathbf{A}^{-1} \left(\frac{\partial \mathbf{A}}{\partial m_i} \mathbf{E}_2 \right) \\
\frac{\partial Z_{yy}}{\partial m_i} &= -{}^1\boldsymbol{\gamma}_{j\ yy}^T \mathbf{A}^{-1} \left(\frac{\partial \mathbf{A}}{\partial m_i} \mathbf{E}_1 \right) - {}^2\boldsymbol{\gamma}_{j\ yy}^T \mathbf{A}^{-1} \left(\frac{\partial \mathbf{A}}{\partial m_i} \mathbf{E}_2 \right) \\
\frac{\partial T_x}{\partial m_i} &= -{}^1\boldsymbol{\gamma}_{j\ T_x}^T \mathbf{A}^{-1} \left(\frac{\partial \mathbf{A}}{\partial m_i} \mathbf{E}_1 \right) - {}^2\boldsymbol{\gamma}_{j\ T_x}^T \mathbf{A}^{-1} \left(\frac{\partial \mathbf{A}}{\partial m_i} \mathbf{E}_2 \right) \\
\frac{\partial T_y}{\partial m_i} &= -{}^1\boldsymbol{\gamma}_{j\ T_y}^T \mathbf{A}^{-1} \left(\frac{\partial \mathbf{A}}{\partial m_i} \mathbf{E}_1 \right) - {}^2\boldsymbol{\gamma}_{j\ T_y}^T \mathbf{A}^{-1} \left(\frac{\partial \mathbf{A}}{\partial m_i} \mathbf{E}_2 \right),
\end{aligned} \tag{3.19}$$

with

$$\begin{aligned}
{}^1\boldsymbol{\gamma}_{j\ xx}^T &= C \left[(\tilde{H}_{x1}\tilde{H}_{y2} - \tilde{H}_{x2}\tilde{H}_{y1})(-\tilde{H}_{y2}^e \boldsymbol{\eta}_{j(x)}^T + \tilde{E}_{x2}^h \boldsymbol{\eta}_{j(y)}^T) \right. \\
&\quad \left. + (\tilde{E}_{x1}\tilde{H}_{y2} - \tilde{E}_{x2}\tilde{H}_{y1})(-\tilde{H}_{x2}^h \boldsymbol{\eta}_{j(y)}^T + \tilde{H}_{y2}^h \boldsymbol{\eta}_{j(x)}^T) \right] \\
{}^2\boldsymbol{\gamma}_{j\ xx}^T &= C \left[(\tilde{H}_{x1}\tilde{H}_{y2} - \tilde{H}_{x2}\tilde{H}_{y1})(-\tilde{E}_{x1}^h \boldsymbol{\eta}_{j(y)}^T + \tilde{H}_{y1}^e \boldsymbol{\eta}_{j(x)}^T) \right. \\
&\quad \left. + (\tilde{E}_{x1}\tilde{H}_{y2} - \tilde{E}_{x2}\tilde{H}_{y1})(-\tilde{H}_{y1}^h \boldsymbol{\eta}_{j(x)}^T + \tilde{H}_{x1}^h \boldsymbol{\eta}_{j(y)}^T) \right] \\
{}^1\boldsymbol{\gamma}_{j\ xy}^T &= C \left[(\tilde{H}_{x1}\tilde{H}_{y2} - \tilde{H}_{x2}\tilde{H}_{y1})(-\tilde{E}_{x2}^h \boldsymbol{\eta}_{j(x)}^T + \tilde{H}_{x2}^e \boldsymbol{\eta}_{j(y)}^T) \right. \\
&\quad \left. + (\tilde{E}_{x2}\tilde{H}_{x1} - \tilde{E}_{x1}\tilde{H}_{x2})(-\tilde{H}_{x2}^h \boldsymbol{\eta}_{j(y)}^T + \tilde{H}_{y2}^h \boldsymbol{\eta}_{j(x)}^T) \right] \\
{}^2\boldsymbol{\gamma}_{j\ xy}^T &= C \left[(\tilde{H}_{x1}\tilde{H}_{y2} - \tilde{H}_{x2}\tilde{H}_{y1})(-\tilde{H}_{x1}^e \boldsymbol{\eta}_{j(x)}^T + \tilde{E}_{x1}^h \boldsymbol{\eta}_{j(y)}^T) \right. \\
&\quad \left. + (\tilde{E}_{x2}\tilde{H}_{x1} - \tilde{E}_{x1}\tilde{H}_{x2})(-\tilde{H}_{y1}^h \boldsymbol{\eta}_{j(x)}^T + \tilde{H}_{x1}^h \boldsymbol{\eta}_{j(y)}^T) \right] \\
{}^1\boldsymbol{\gamma}_{j\ yx}^T &= C \left[(\tilde{H}_{x1}\tilde{H}_{y2} - \tilde{H}_{x2}\tilde{H}_{y1})(-\tilde{H}_{y2}^e \boldsymbol{\eta}_{j(y)}^T + \tilde{E}_{y2}^h \boldsymbol{\eta}_{j(x)}^T) \right. \\
&\quad \left. + (\tilde{E}_{y1}\tilde{H}_{y2} - \tilde{E}_{y2}\tilde{H}_{y1})(-\tilde{H}_{x2}^h \boldsymbol{\eta}_{j(y)}^T + \tilde{H}_{y2}^h \boldsymbol{\eta}_{j(x)}^T) \right] \\
{}^2\boldsymbol{\gamma}_{j\ yx}^T &= C \left[(\tilde{H}_{x1}\tilde{H}_{y2} - \tilde{H}_{x2}\tilde{H}_{y1})(-\tilde{E}_{y1}^h \boldsymbol{\eta}_{j(y)}^T + \tilde{H}_{y1}^e \boldsymbol{\eta}_{j(x)}^T) \right. \\
&\quad \left. + (\tilde{E}_{y1}\tilde{H}_{y2} - \tilde{E}_{y2}\tilde{H}_{y1})(-\tilde{H}_{y1}^h \boldsymbol{\eta}_{j(x)}^T + \tilde{H}_{x1}^h \boldsymbol{\eta}_{j(y)}^T) \right]
\end{aligned} \tag{3.20}$$

$$\begin{aligned}
{}^1\boldsymbol{\gamma}_{j\text{yy}}^T &= C \left[(\tilde{H}_{x1}\tilde{H}_{y2} - \tilde{H}_{x2}\tilde{H}_{y1})(-\tilde{E}_{y2}^h \boldsymbol{\eta}_{j(x)}^T + \tilde{H}_{x2}^e \boldsymbol{\eta}_{j(x)}^T) \right. \\
&\quad \left. + (\tilde{E}_{y2}\tilde{H}_{x1} - \tilde{E}_{y1}\tilde{H}_{x2})(-\tilde{H}_{x2}^h \boldsymbol{\eta}_{j(y)}^T + \tilde{H}_{y2}^h \boldsymbol{\eta}_{j(x)}^T) \right] \\
{}^2\boldsymbol{\gamma}_{j\text{yy}}^T &= C \left[(\tilde{H}_{x1}\tilde{H}_{y2} - \tilde{H}_{x2}\tilde{H}_{y1})(-\tilde{H}_{x1}^e \boldsymbol{\eta}_{j(y)}^T + \tilde{E}_{y1}^h \boldsymbol{\eta}_{j(x)}^T) \right. \\
&\quad \left. + (\tilde{E}_{y2}\tilde{H}_{x1} - \tilde{E}_{y1}\tilde{H}_{x2})(-\tilde{H}_{y1}^h \boldsymbol{\eta}_{j(x)}^T + \tilde{H}_{x1}^h \boldsymbol{\eta}_{j(y)}^T) \right]
\end{aligned}$$

and

$$\begin{aligned}
{}^1\boldsymbol{\gamma}_{j\text{T}_x}^T &= C \left[(\tilde{H}_{x1}\tilde{H}_{y2} - \tilde{H}_{x2}\tilde{H}_{y1})(-\tilde{H}_{y2}^h \boldsymbol{\eta}_{j(z)}^T + \tilde{H}_{z2}^h \boldsymbol{\eta}_{j(y)}^T) \right. \\
&\quad \left. + (\tilde{H}_{z1}\tilde{H}_{y2} - \tilde{H}_{z2}\tilde{H}_{y1})(-\tilde{H}_{x2}^h \boldsymbol{\eta}_{j(y)}^T + \tilde{H}_{y2}^h \boldsymbol{\eta}_{j(x)}^T) \right] \\
{}^2\boldsymbol{\gamma}_{j\text{T}_x}^T &= C \left[(\tilde{H}_{x1}\tilde{H}_{y2} - \tilde{H}_{x2}\tilde{H}_{y1})(-\tilde{H}_{z1}^h \boldsymbol{\eta}_{j(y)}^T + \tilde{H}_{y1}^h \boldsymbol{\eta}_{j(z)}^T) \right. \\
&\quad \left. + (\tilde{H}_{z1}\tilde{H}_{y2} - \tilde{H}_{z2}\tilde{H}_{y1})(-\tilde{H}_{y1}^h \boldsymbol{\eta}_{j(x)}^T + \tilde{H}_{x1}^h \boldsymbol{\eta}_{j(y)}^T) \right] \\
{}^1\boldsymbol{\gamma}_{j\text{T}_y}^T &= C \left[(\tilde{H}_{x1}\tilde{H}_{y2} - \tilde{H}_{x2}\tilde{H}_{y1})(-\tilde{H}_{z2}^h \boldsymbol{\eta}_{j(x)}^T + \tilde{H}_{x2}^h \boldsymbol{\eta}_{j(z)}^T) \right. \\
&\quad \left. + (\tilde{H}_{z2}\tilde{H}_{x1} - \tilde{H}_{z1}\tilde{H}_{x2})(-\tilde{H}_{x2}^h \boldsymbol{\eta}_{j(y)}^T + \tilde{H}_{y2}^h \boldsymbol{\eta}_{j(x)}^T) \right] \\
{}^2\boldsymbol{\gamma}_{j\text{T}_y}^T &= C \left[(\tilde{H}_{x1}\tilde{H}_{y2} - \tilde{H}_{x2}\tilde{H}_{y1})(-\tilde{H}_{x1}^h \boldsymbol{\eta}_{j(z)}^T + \tilde{H}_{z1}^h \boldsymbol{\eta}_{j(x)}^T) \right. \\
&\quad \left. + (\tilde{H}_{z2}\tilde{H}_{x1} - \tilde{H}_{z1}\tilde{H}_{x2})(-\tilde{H}_{y1}^h \boldsymbol{\eta}_{j(x)}^T + \tilde{H}_{x1}^h \boldsymbol{\eta}_{j(y)}^T) \right],
\end{aligned} \tag{3.21}$$

where $C = (\tilde{H}_{x1}\tilde{H}_{y2} - \tilde{H}_{x2}\tilde{H}_{y1})^{-2}$. Note, that equations 3.20 were originally stated in Newman and Alumbaugh (2000), were the expressions for ${}^2\boldsymbol{\gamma}_{j\text{xy}}^T$, ${}^2\boldsymbol{\gamma}_{j\text{yx}}^T$, ${}^1\boldsymbol{\gamma}_{j\text{yy}}^T$ contain an index mistake each that was corrected here.

Per datum d_n and model parameter m_i we obtain

$$\frac{\partial d_n}{\partial m_i} = -{}^1\boldsymbol{\gamma}_n^T \mathbf{A}^{-1} \left(\frac{\partial \mathbf{A}}{\partial m_i} \mathbf{E}_1 \right) - {}^2\boldsymbol{\gamma}_n^T \mathbf{A}^{-1} \left(\frac{\partial \mathbf{A}}{\partial m_i} \mathbf{E}_2 \right) \quad \begin{array}{l} \forall i = 1 \dots M \\ \forall n = 1 \dots N. \end{array} \tag{3.22}$$

Inserting the expression for $\partial d_n / \partial m_i$ into the data misfit gradient (eq. 2.14) we obtain

$$\begin{aligned}
\nabla \Phi_d(\mathbf{m}) &= \frac{\partial \Phi_d}{\partial m_i} \\
&= -2\text{Re} \left[-\sum_{n=1}^N (\Delta d_n)^* {}^1\boldsymbol{\gamma}_n^T \mathbf{A}^{-1} \left(\frac{\partial \mathbf{A}}{\partial m_i} \mathbf{E}_1 \right) - \sum_{n=1}^N (\Delta d_n)^* {}^2\boldsymbol{\gamma}_n^T \mathbf{A}^{-1} \left(\frac{\partial \mathbf{A}}{\partial m_i} \mathbf{E}_2 \right) \right] \\
&= -2\text{Re} \left[{}^1\boldsymbol{\Gamma}^T \mathbf{A}^{-1} \left(\frac{\partial \mathbf{A}}{\partial m_i} \mathbf{E}_1 \right) + {}^2\boldsymbol{\Gamma}^T \mathbf{A}^{-1} \left(\frac{\partial \mathbf{A}}{\partial m_i} \mathbf{E}_2 \right) \right]
\end{aligned} \tag{3.23}$$

with

$${}^1\mathbf{\Gamma}^T = -2 \sum_{n=1}^N (\Delta d_n)^* {}^1\boldsymbol{\gamma}_n^T \quad \text{and} \quad {}^2\mathbf{\Gamma}^T = -2 \sum_{n=1}^N (\Delta d_n)^* {}^2\boldsymbol{\gamma}_n^T. \quad (3.24)$$

As inverting \mathbf{A} is expensive, the products ${}^1, {}^2\mathbf{\Gamma}^T \mathbf{A}^{-1}$ are obtained via solving two pseudo-forward problems

$$\begin{aligned} {}^1\mathbf{\Gamma}^T \mathbf{A}^{-1} &= {}^1\mathbf{v}^T & \Leftrightarrow \mathbf{A} {}^1\mathbf{v} &= {}^1\mathbf{\Gamma}, \\ {}^2\mathbf{\Gamma}^T \mathbf{A}^{-1} &= {}^2\mathbf{v}^T & \Leftrightarrow \mathbf{A} {}^2\mathbf{v} &= {}^2\mathbf{\Gamma}. \end{aligned} \quad (3.25)$$

for ${}^1\mathbf{v}$ and ${}^2\mathbf{v}$.

A model parameter transformation bounded by lower (ρ^{min}) and upper resistivities (ρ^{max})

$$m_i = \ln \left(\frac{\rho_i - \rho^{min}}{\rho^{max} - \rho_i} \right), \quad \rho^{min} < \rho_i < \rho^{max}, \quad (3.26)$$

is applied. The data gradients are derived w.r.t. the transformed model parameters, which involves application of the chain rule, where

$$\frac{\partial}{\partial m_i} = \frac{\partial}{\partial \rho_i} \frac{\partial \rho_i}{\partial m_i} \quad (3.27)$$

and

$$\frac{\partial \rho_i}{\partial m_i} = \frac{(\rho^{max} - \rho_i)(\rho_i - \rho^{min})}{(\rho^{max} - \rho^{min})}. \quad (3.28)$$

3.2.2 Model regularisation for tetrahedral meshes

As introduced in Section 2.5.2, the inversion approach applied in this work is of a regularised nature. Thus, the inverse model covariance matrix \mathbf{C}_m^{-1} has to be computed (eq. 2.12). It is common to define the inverse model covariance matrix \mathbf{C}_m^{-1} as a smoothing operator (Tikhonov and Arsenin, 1977; Constable et al., 1987), expressed as a product $\mathbf{L}^T \mathbf{L}$. Three different regularisation schemes are implemented: i) smoothness constraints via absolute differences between model parameters, ii) smoothness constraints via a gradient approximation and iii) minimum norm regularisation with a reference model (e.g. Grayver et al., 2013). Additionally, structural weights can be applied to the model covariance matrix increasing or decreasing the smoothing across element faces in certain model regions. For all implemented schemes, the model covariance matrix is sparse and saved in sparse COO format to save memory.

Absolute differences

The smoothness matrix \mathbf{L} for unstructured tetrahedral meshes is constructed as outlined in Günther et al. (2006). Taking the neighbouring element relations into account, two neighbouring elements i and t share a face s . Accordingly, the sparse matrix \mathbf{L} contains $2S$ entries, where S is the number of inner boundaries, i.e. faces between elements. \mathbf{L} is of size $[S \times M]$, where M is the number of free inversion model parameters. The entries of \mathbf{L} are:

$$L_{s,i} = -1, \quad (3.29)$$

$$L_{s,t} = 1. \quad (3.30)$$

\mathbf{L} does not have to be computed explicitly, but rather $\mathbf{L}^T \mathbf{L}$, which is of size $[M \times M]$. The corresponding entries of $\mathbf{L}^T \mathbf{L}$ are:

$$L^T L_{i,i} = L^T L_{t,t} = \text{number of adjacent elements (1 to 4)}, \quad (3.31)$$

$$L^T L_{i,t} = -1, \quad (3.32)$$

$$L^T L_{t,i} = -1. \quad (3.33)$$

$\mathbf{L}^T \mathbf{L}$ is symmetric and sparse (Fig. 3.3).

Gradient approximation via weighted sum of squares

The model regularisation term is set up as outlined in Key (2016) for 2-D inversion and expanded with the third dimension. The method is a weighted sum of squares approach. It approximates the two-norm of the gradient of the model parameters taking a volume weighted average of absolute differences between all parameters, without calculating the model gradients explicitly.

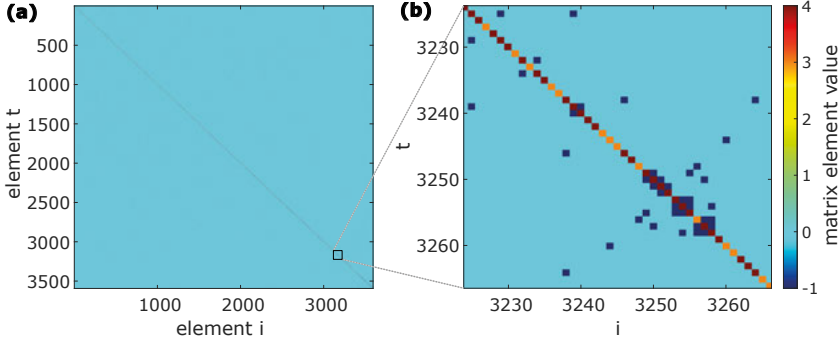


Figure 3.3. Example of a smoothing matrix $\mathbf{L}^T \mathbf{L}$ (a) and zoom into the full matrix (b), when homogeneous absolute difference smoothing is used.

Structural weights

The absolute differences and the gradient approximation approach can be advanced by applying structural weights to the smoothing operator. The structural weights control the smoothing across cell boundaries individually by amplifying or de-amplifying the strength of the smoothness constraints in \mathbf{L} . The structural weights are implemented as a diagonal weighting matrix $\mathbf{w} = \text{diag}(w_s)$ (Rücker, 2011), which is multiplied from the left to \mathbf{L} :

$$\mathbf{L}_1 = \text{diag}(w_s) \mathbf{L} \quad \text{for } s = 1, \dots, S. \quad (3.34)$$

Three options for constructing the weighting matrix \mathbf{w} , i.e. defining its entries w_s are implemented:

1. If locations of sharp lithological contrasts in the model are known prior to the inversion from boreholes, geo-radar or seismic measurements, the inversion mesh can be designed, such that inner faces are aligned with the expected contrasts, i.e. interfaces are dividing different model regions. Then, the weights w_s of the element faces constituting these structural boundaries can be reduced to allow for rough resistivity transitions in the model across the expected contrasts. Model region numbers and a user-defined weight < 1 have to be provided as input parameters.
2. Anisotropic constraints (e.g. lower weights on horizontal compared to vertical boundaries), if a layered subsurface is expected, are implemented as described in Rücker (2011). To run an inversion with anisotropic structural weighting, vertical and horizontal weights have to be provided.
3. A distance-to-source weighting function (cf. **Paper III**) aims at avoiding the appearance of resistivity artefacts close to source locations. Therefore, smoothing across model faces is applied, i.e. the entries w_s are gradually increasing from the target area towards the source locations.

3.2.3 Lagrange multiplier

The regularisation parameter λ , also called Lagrange multiplier, controls the amount of model regularisation in the objective function (eq. 2.12). In case smoothing regularisation is applied, small values for λ lead to rough models, whereas large values produce smooth models (Fig. 3.4). λ is a user-defined input parameter and is fixed over all iterations for NLCG inversion. For a fixed λ , the global minimum of the objective function is stationary. Compared to inversion approaches, where λ is automatically adjusted during the inversion procedure, a bad choice of λ for NLCG inversion is prone to guide the inversion towards not fitting the data properly. A good choice of λ leads to a data fit within the range of the specified data uncertainties and regularisation constraints.

One way to find an optimal λ is to apply the L-curve method (Hansen and O’Leary, 1993; Günther et al., 2006) for a specific data set, start model and regularisation approach; The data misfit term Φ_d is depicted against the model regularisation term Φ_m (eq. 2.12) for a series of different λ . The optimum λ is found at the maximum curvature of the resulting L-shaped curve. However, for this method, a large number of inversion runs with different λ has to be performed. Therefore, for the inversions conducted in this work (**Papers III and IV**), optimal λ are determined by investigating the convergence curves of the Root Mean Square error (RMS) and of the objective function ($\Phi = \Phi_d + \lambda \Phi_m$) for a small number of different λ (exemplary shown in Fig. 3.4). For each model, the largest λ resulting in the smallest RMS alongside steady convergence of the objective function is chosen. Note, that in between the different implemented model regularisation approaches (cf. Sec. 3.2.2), the values for λ can vary by orders of magnitude, as the amplitudes of the regularisation matrix entries can differ strongly between the methods.

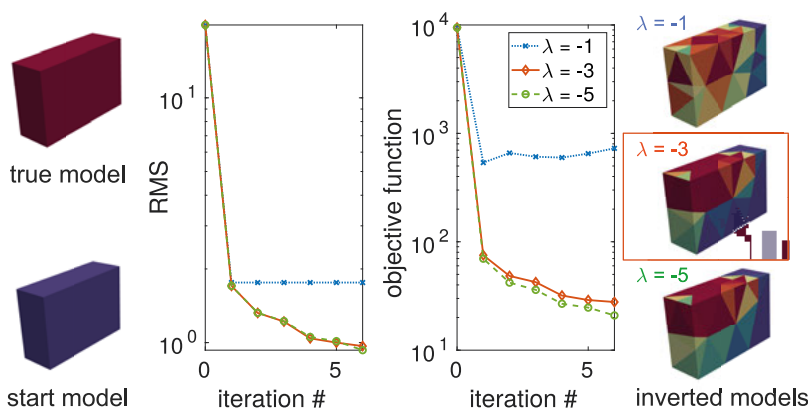


Figure 3.4. Example convergence curves (RMS and objective function) for different Lagrange multipliers λ (expressed in \log_{10} -values, preferred value $\lambda = -3$) and corresponding models.

3.2.4 Source locations

In the numerical formulation of the forward problem (eq. 2.11), the source currents are directly included at the source locations, i.e. at the corresponding DOF. In the models presented in the papers of this thesis, the sources are modelled as extended horizontal electric bipoles/dipoles (HEDs) or as horizontal magnetic dipoles (HMDs) realised via vertical loops. Magnetic sources are purely inductively coupled to the subsurface, whereas electric bipole sources are additionally galvanically coupled to the subsurface through the grounding of the bipole endpoints, i.e. the source electrodes. The source locations have to be handled with caution, not only in the total-field approach forward modelling (cf. Appendix A4 in **Paper I**), but also in the inversion process. For example, if the resistivities of neighbouring cells below the source are updated during the inversion and, consequently, differ from each other. Additionally, it is observed in Example II of **Paper III** that polarity changes in the data gradients are present at the locations of the source electrodes, which produces, in this example, strong artefacts in the resistivity model. In case source segments are located at the surface, a thin, fixed layer can be included right below the source to prevent the inversion from changing the resistivity model there. Grayver et al. (2013) apply the same concept for a primary/secondary field approach.

Here I present an additional study utilising the synthetic model of **Paper IV** (cf. Sec. 4.4) that comprises a half space of $100\ \Omega\text{m}$ with two embedded conductive anomalies ($5\ \Omega\text{m}$). The study investigates the gradient pattern of the objective function for the start model as well as the convergence behaviour and resistivity models for two cases: In Case A, the free model parameter region starts directly below the surface (Fig. 3.6a). In Case B, a fixed layer with the true model resistivity is included right below the surface (Fig. 3.6e). For both cases, transfer functions (Z_{xy} , Z_{yx} , T_x , T_y) are used as input data.

As already observed in **Paper IV**, high absolute values and a polarity change of data gradients are present in the vicinity of the source (Fig. 3.6b, f), not along the extended source cables, but mainly at the source electrodes. If a fixed layer is included below the surface, data gradient amplitudes are high exactly below this layer, but of smaller amplitudes than at the surface (Fig. 3.6f). Therefore, the start model of $200\ \Omega\text{m}$ is very likely to be changed in the vicinity of the source electrodes by the inversion, especially, because the implemented regularisation approaches (cf. Sec. 3.2.2) do not apply smoothing towards the fixed outer model region.

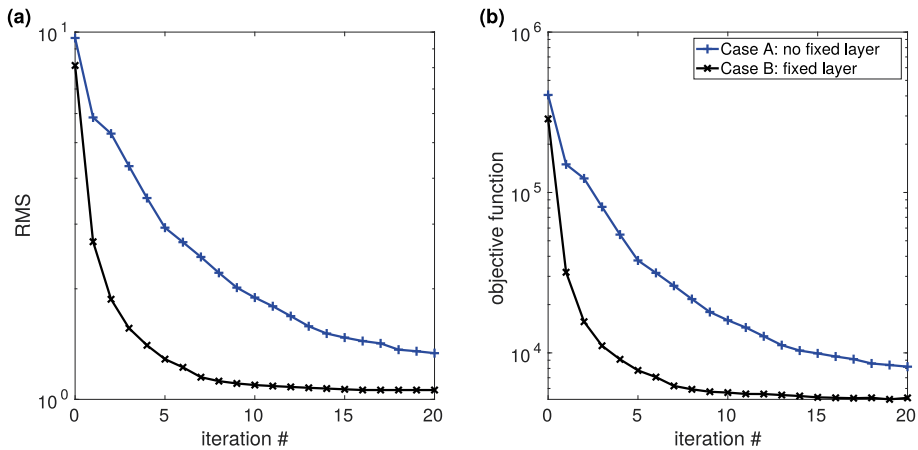


Figure 3.5. Convergence rates of transfer function inversions producing the models shown in Figure 3.6.

The convergence curves of Case A and B (Fig. 3.5) can not easily be compared, as Case A comprises more model parameters and has a slightly higher start RMS than Case B. However, Case B converges in substantially fewer iterations than Case A.

Investigating the resulting resistivity models at the top of the free model region (Fig. 3.6c and g), small-scale artefacts can be observed at the source electrodes for both cases. The artefacts are more pronounced for Case A. However, they do not appear along the extended source lines. In Case B, the background resistivity in the upper part of the model as well as the anomalies are better reproduced than in Case A (Fig. 3.6d and h). The latter might be, because Case A has not converged within the 20 iterations it was run (cf. Fig. 3.5).

It can be concluded that, if the resistivity distribution of the upper subsurface below transmitters is well known, it can be helpful to include it in the start model and fix this region during inversion. However, the fixed layer can be problematic when inverting real field data, as unknown inhomogeneities in the source vicinity cannot be accounted for in the start model. Therefore, Commer and Newman (2008) apply an advanced method called source signature correction, which is advisable to be implemented in the inversion code in the future. Additionally, the study can be extended for EM field component inversion.

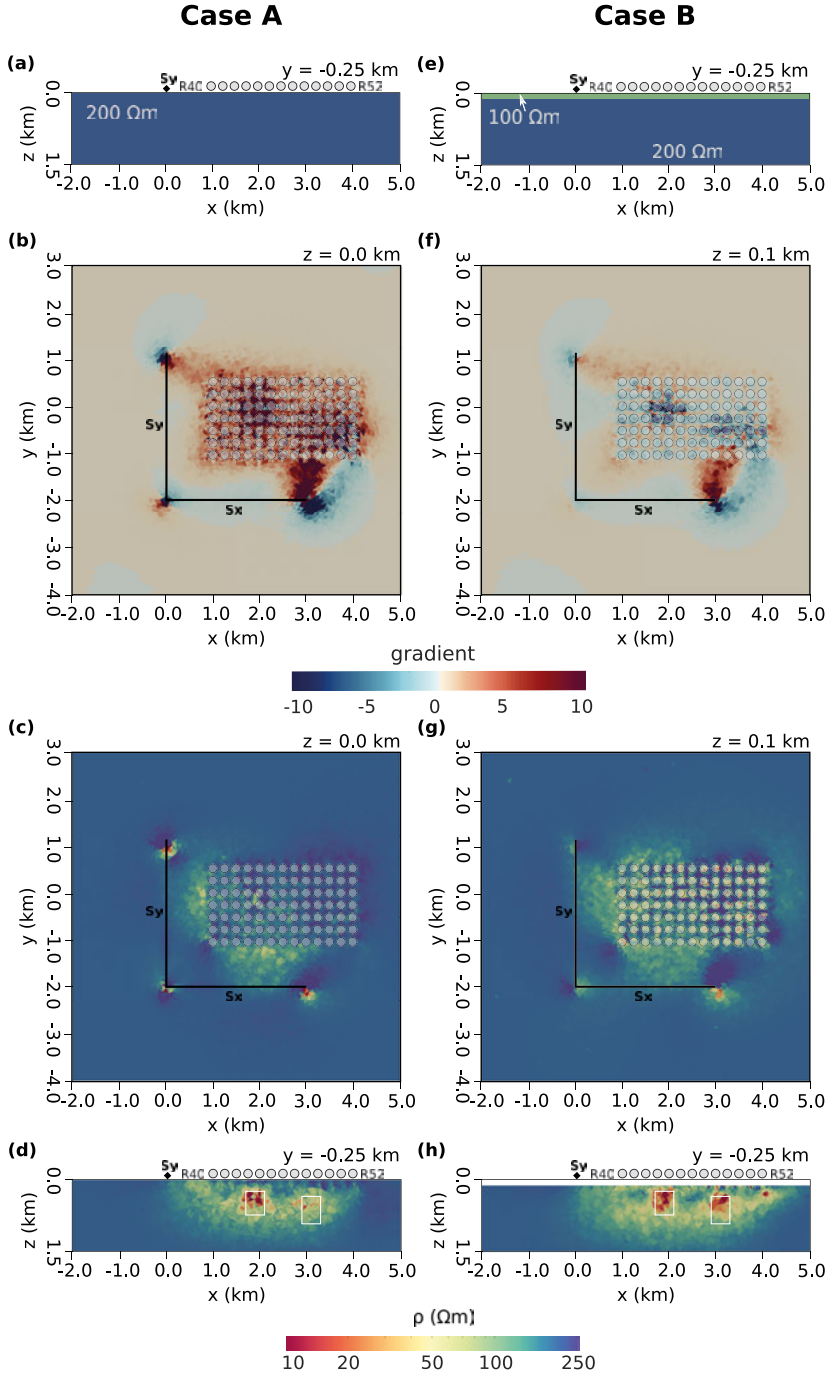


Figure 3.6. Models with two different options of source inclusion using transfer functions as input data. Case A: the free model parameter region starts directly below the surface. Case B: a fixed layer with the true model resistivity is included right below the surface. Start models (a,e), gradients of the objective function for the start model (b,f) and resistivity models with outlines of conductive anomalies (c,d,g,h).

4. Summary of papers

In this chapter, comprehensive summaries of the four papers included in this thesis are provided alongside some background information and comments. In addition to methodological details, the papers contain application examples of the codes described in the previous chapters. Note, that no figures from **Paper I** and **Paper II** are duplicated for the summaries, but the reader is encouraged to have a look into the published versions.

4.1 Paper I

Efficient goal-oriented mesh refinement in 3-D finite-element modelling adapted for controlled source electromagnetic surveys

4.1.1 Motivation

3-D forward modelling and inversion software is required to obtain reliable subsurface models from EM data acquired above complex subsurface structures. The expectations of 3-D simulations are twofold: On the one hand, complex 3-D geometries of both the subsurface and the measurement setup should be physically correctly modelled to obtain better images of the subsurface compared to what is possible with 1-D or 2-D simulations. On the other hand, the computational problem should be performed in an adequate time and with satisfying accuracy, even though 3-D simulations require much more computer resources than 1-D or 2-D problems. Thus, the key objective for 3-D simulations is to obtain accurate results while keeping memory consumption and run times as low as possible. This objective becomes particularly important as the main purpose of forward modelling codes is to use them within an inversion framework, where forward problems have to be solved in each iteration. Thus, the faster one forward calculation is, the faster will be an inversion procedure.

4.1.2 Summary

A 3-D CSEM forward modelling algorithm is developed to enable the simulation of EM fields for challenging subsurface scenarios and measurement setups. The code incorporates a goal-oriented adaptive mesh refinement option to automatically improve input meshes aiming at finding a good trade-off

between solution accuracy at the receiver stations and the problem size. The article presents the implementation, mesh refinement procedure and validation of the 3-D FE forward modelling code. The main steps of the FE forward modelling procedure are summarised in Figure 4.1.

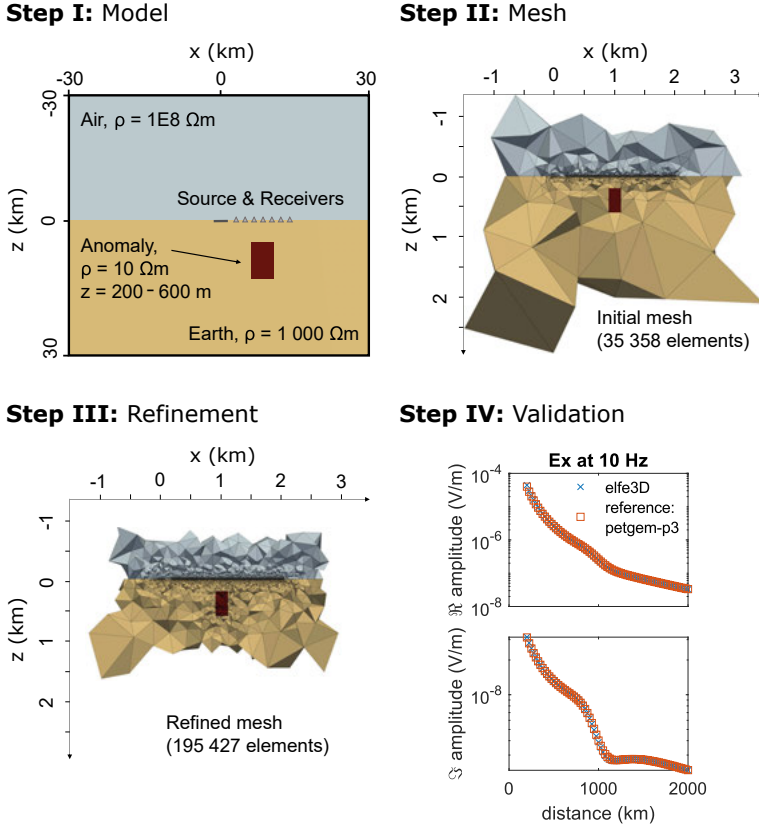


Figure 4.1. Key steps of the FE forward modelling procedure including the choice of a subsurface model and source-receiver setup (Step I), the initial meshing of the modelling domain (Step II), the mesh refinement (Step III) and the validation against a reference solution (Step IV). The reference solution for this example was computed with PETGEM (Castillo-Reyes et al., 2018) using third order interpolation functions.

The code applies a total electric field approach and uses tetrahedral elements and unstructured meshes combined with linear edge-based interpolation functions, which enables accurate discretisation of topography, anomalies and elongated extended sources. Variable material properties are isotropic electrical resistivity and magnetic permeability. Dirichlet boundary conditions terminate the modelling domain and a direct solver is used to solve the system of equations. The algorithm is implemented in modern Fortran using automatic vectorisation and shared-memory parallelisation with OpenMP. The implemented goal-oriented automatic mesh refinement strategy constructs problem-

specific meshes to minimise problem sizes. Therefore, an adjoint problem specifically for CSEM modelling is set up. Furthermore, published approaches for error estimation are adapted to work for CSEM problems.

The forward algorithm and the implemented adaptive mesh refinement approach are verified by comparing the forward responses for a half space model and a layered model to semi-analytic 1-D solutions. Furthermore, forward responses for a 3-D model are compared to solutions obtained with a second-order FE code (`custEM`, Rochlitz et al., 2019). Additionally, the article contains a feasibility study for CSEM measurements across ferrous mineral deposits in central Sweden.

4.1.3 Remarks

After publishing **Paper I**, the standalone version of the forward modelling code was named `elfe3D` (modelling with the total **e**lectric field approach using **f**inite **e**lements in **3-D**). The forward problems presented in **Paper I** were solved with the direct solver PARDISO (Alappat et al., 2020; Bollhöfer et al., 2020, 2019), which was implemented at first in the `elfe3D` code. Later, the options for solving the system of equations were extended by including calls to the comparable direct solver MUMPS (Amestoy et al., 2001). Furthermore, variable dielectric permittivity was included in the boundary value problem solved by `elfe3D`. Now, scenarios, where displacement currents are present due to a very resistive subsurface in combination with high frequencies, can be simulated. On top of the examples presented in **Paper I**, `elfe3D` was applied and improved to enable the modelling of subsurface scenarios which include steel-cased wells represented as perfect electric conductors (cf. **Paper II**). Furthermore, forward responses for a model with topography were obtained for comparison with a spectral element (SE) code that uses higher order interpolation functions (Weiss et al., 2023a). The forward responses of both numerical schemes are in good agreement, which cross-validates the capability of `elfe3D` to model scenarios with topography. In line with publications about FE codes using higher order interpolation schemes (e.g. Schwarzbach et al., 2011; Grayver and Kolev, 2015; Rochlitz et al., 2019), Weiss et al. (2023a) state that 2nd or 3rd order polynomial interpolation functions are superior to linear polynomial interpolation functions. Therefore, it is planned as a future development to include higher order interpolation functions into `elfe3D` and to adapt the implemented mesh refinement accordingly.

4.2 Paper II

Meshing strategies for 3-D geo-electromagnetic modelling in the presence of metallic infrastructure

4.2.1 Motivation

A problem-specific mesh is one of the most important ingredients to obtain accurate solutions for discrete 3-D simulations. However, generating such a mesh is also one of the most challenging and time-consuming tasks in the modelling process. This lesson is best learned by developing and applying modelling code, because each setup has its specific features that have to be included in a mesh.

The source and receiver locations, but also topography or complex-shaped subsurface features, need to be discretised with caution. An example is man-made infrastructure that is often metallic and of very different scales compared to the surrounding geological features. Therefore, it can influence the local EM fields quite drastically (e.g. Streich and Swidinsky, 2023).

4.2.2 Summary

Paper II investigates how CSEM models including small-scale conductive infrastructure can be wisely discretised and simulated. Steel-cased wells, which are relevant to include in modelling of many exploration CSEM settings, are used as an example for such infrastructure. The wells have to be taken into account when simulating the EM fields as they are highly conductive. Discretising models with wells is challenging due to the different scales characterised by thin, long boreholes and large-scale geological formations. Several methods have already been proposed to effectively model steel-cased wells. In this work, the focus lies on the representation of steel-cased wells as perfect electric conductors (PEC). As visualised in Figure 4.2, a metallic cased well can be either represented by a replacement prism, a combination of prism and PEC or by a PEC only (Um et al., 2020). The PEC is implemented like a boundary condition on mesh edges. It reduces problem sizes significantly as no tiny elements are needed to discretise a few centimetre thick prism. Meshes can be constructed, such that an arbitrary orientation of the wells is possible.

Two 3-D forward modelling codes, `elfe3D` and `PETGEM` (Castillo-Reyes et al., 2018), are used in this collaborative work. `elfe3D` includes goal-oriented automatic mesh refinement and `PETGEM` supports higher-order basis functions. Both methods are combined. The goal-oriented refinement technique and subsequent higher-order simulations are applied for two test models, which require different versions of approximating metallic-cased wells.

The study indicates that the goal-oriented refinement deals well with PEC approximations, but has its difficulties with prism and PEC combinations (Fig. 4.2). Optimal solutions for in-line and cross-line forward responses

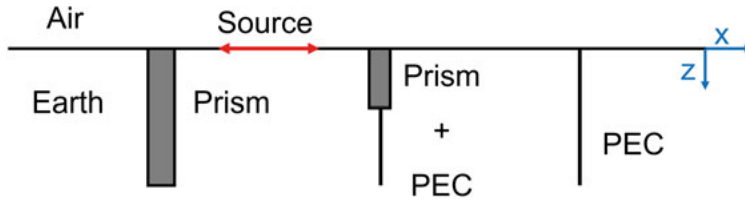


Figure 4.2. Simplified options for approximating a metallic-cased well.

can be achieved by using goal-oriented refinement together with 2nd order elements. Additionally, the same accuracy cannot be obtained with globally fine high quality meshes, which demonstrates the effectiveness of the refinement method. The modelling tests result in meshing and modelling recommendations useful for the EM modelling community.

4.2.3 Comment

Further forward modelling studies of PEC and prism approximations for boreholes revealed that the validity of these numerical simplifications strongly depends on the subsurface resistivities, the measurement setup and the frequency range used. PEC approximations can easily result in more than 10% difference to a full prism representation of a borehole, which is an approximation of a hollow-borehole casing by itself. Additionally, borehole casings can also exhibit a magnetic permeability contrast to the surrounding geology, which is important to include in the numerical simulations of EM surveys with steel infrastructure (Heagy and Oldenburg, 2023). In general, the use of PEC approximations leads to enormous reductions in problem sizes compared to modelling boreholes with hollow casings or prisms. It can be recommended to study the accuracy of the approach for every setting. If one can quantify the accuracy that is lost with PEC approximations, it can be taken into account in an inversion by modifying the data uncertainties. In this way, PEC approximations can be useful not only for modelling boreholes, but also other steel infrastructure such as pipelines.

4.3 Paper III

Three-dimensional electromagnetic inversion of transfer function data from controlled sources

4.3.1 Motivation

Although a number of 3-D frequency-domain CSEM inversion codes exist (e.g. Haber et al., 2004; Newman and Boggs, 2004; Mackie et al., 2007; Gribenko and Zhdanov, 2007; Commer and Newman, 2008; Plessix and Mulder, 2008; Abubakar et al., 2009; Grayver et al., 2013; Kelbert et al., 2014; Bretaudeau and Coppo, 2016; Cao et al., 2016; Heagy et al., 2017; Zhang, 2018; Long et al., 2020; Cai et al., 2021; Kara and Farquharson, 2023; Smirnova et al., 2023; Rochlitz et al., 2023), 3-D inversion is not yet routinely applied and research and developments in the field are currently ongoing.

3-D inverse modelling of EM data constitutes a computationally challenging task (Avdeev, 2005). 1-D or 2-D inversions are certainly the faster methods of choice. To evaluate the reliability of lower-dimensionality inversion models, appraisal tools exist (e.g. Deleersnyder et al., 2022). These tools can be used to identify areas in 1-D or 2-D models that do not fit potential multidimensionality in the observed data. However, 3-D inverse modelling is the only option to evaluate CSEM data containing multidimensionality in a way that an entire data set can be handled by one modelling approach and no intrinsic methodological errors are introduced through reducing a 3-D problem to one or two dimensions.

4.3.2 Summary

Paper III presents implementation details and applications of the developed inversion code that produces 3-D resistivity models of the subsurface from frequency-domain CSEM data. To obtain forward data within the inversion workflow, the 3-D FE forward solver elaborated on in **Paper I** was implemented into the inversion framework *emilia* (Kalscheuer et al., 2008, 2010, 2015). An NLCG inversion approach (Zbinden, 2015) is utilised and impedance tensor components and VMTF generated by a set of two independently oriented horizontal electric bipole or horizontal magnetic dipole sources can be inverted.

The inversion can handle CSEM setups with multiple source locations, topography and arbitrary receiver locations. An inner subset of a tetrahedral forward modelling mesh serves as the inversion domain containing the free model parameters for the inversion, i.e. isotropic electrical resistivities. The convergence of the inversion algorithm is improved with preconditioning. Furthermore, a distance-to-source weighting function is introduced to the implemented regularisation schemes. The weighting aims at preventing large model

updates near sources, where sensitivity concentrations can be present and may produce severe artefacts in the models.

The article shows the application of the inversion code for two synthetic and one field data example. The first synthetic model consists of a regular receiver grid combined with four sets of horizontal electric dipole sources regularly illuminating the block-resistivity anomalies in the model. The second synthetic model simulates a more realistic field setting: an irregular receiver grid above a conductive, inclined resistivity anomaly distant to a single pair of source orientations (Fig. 4.3). This model suffers from heterogeneous illumination of the target and strong sensitivity concentrations near the transmitter. Therefore, the above mentioned weighting function in the regularisation term is tested enforcing a smoother model close to the source location (Fig. 4.4). For the examples presented, the convergence behaviour of the algorithm is satisfying and the models can be reproduced acceptably well.

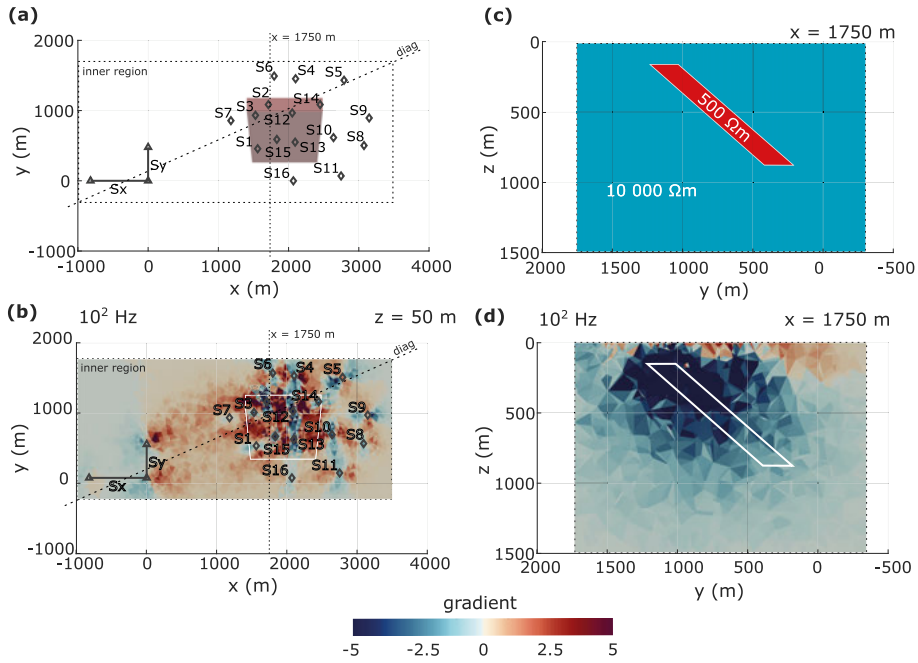


Figure 4.3. Second synthetic modelling example of **Paper III**: measurement setup with transmitter (Sx, Sy) and receiver (S1-S16) locations at the surface (a), data gradients for a start model of 10 000 Ωm at the top of the free model region illustrating the sensitivity distribution (b), true model resistivities at a vertical slice through the central model (c), data gradients for a start model of 10 000 Ωm at a vertical slice through the central model (d). Figure modified from **Paper III**.

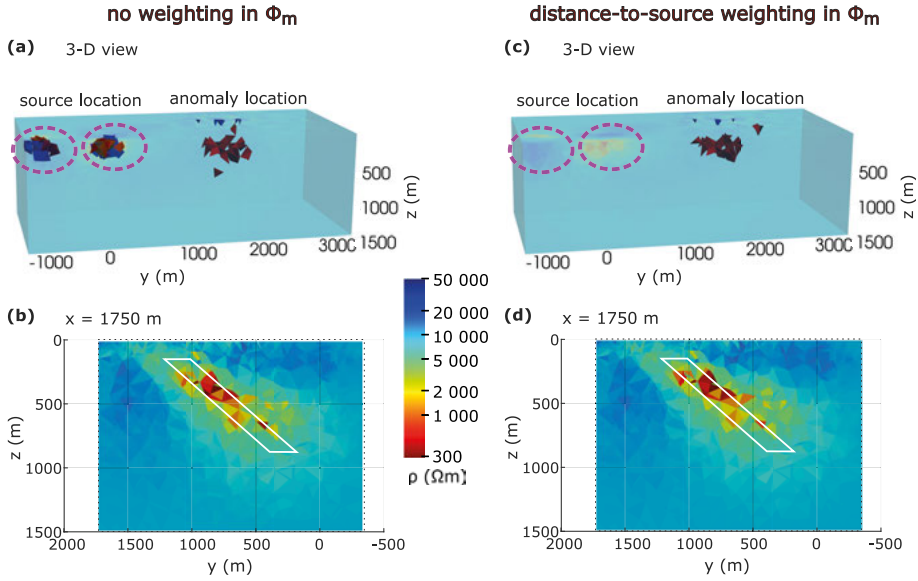


Figure 4.4. Resistivity models of the second synthetic modelling example of **Paper III** with gradient-approximation regularisation (a,b) and gradient-approximation regularisation including a distance-to-source weighting (c,d). The weighting reduces artefacts close to the source electrode locations. Figure modified from **Paper III**. Data and data fit are presented in **Paper III**.

The field data inversion faces the code with challenges that can come along with real data and geological field settings: topography, noisy data that cover only a small frequency range and a single pair of independent source polarisations. The subsurface material distribution involves lake water, sediments, bedrock and fracture zones (Fig. 4.5). The produced models are compared to existing 2-D resistivity models obtained from a combined far-field inversion approach of radio-magnetotelluric (RMT) and CSEM data as well as determinant inversion of RMT data (Fig. 4.6). Due to the limited frequency range of the collected CSEM data and the large model cells, the 3-D models are not able to represent the shallow subsurface in detail. However, the main deep resistivity features are similar to the ones observed in the 2-D models. This further confirms the applicability of the inversion code. A number of improvements for the inversion algorithm are suggested including the usage of higher-order approximations in the forward modelling, the implementation of iterative solution methods and better code parallelisation.

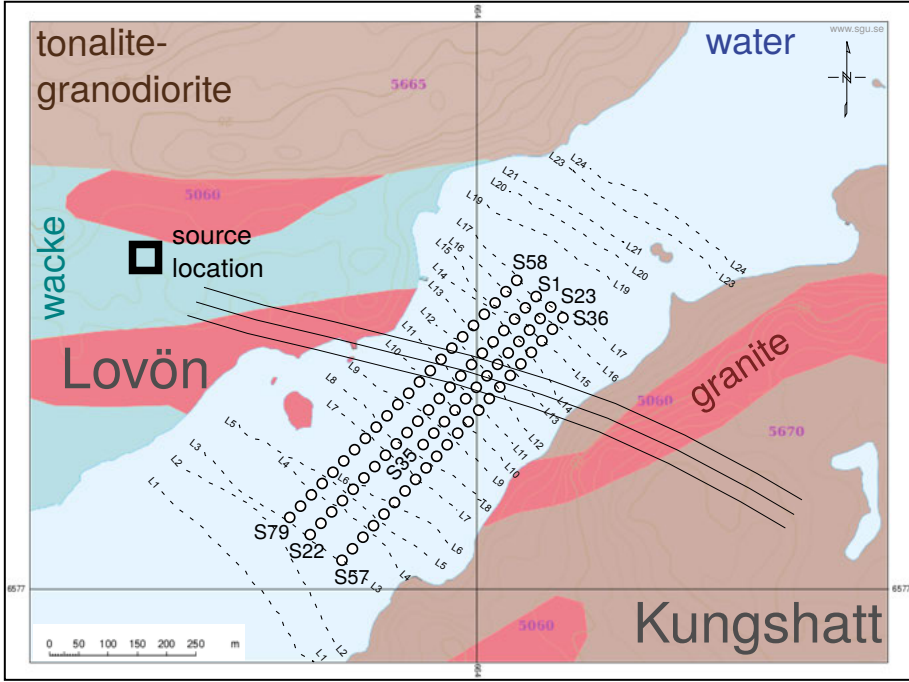


Figure 4.5. Geological map of the study area in Stockholm including the location of the RMT profiles (labelled L#: dashed lines), CSEM measurement locations (labelled S#: dots) and the planned path of the tunnel (parallel solid black lines). Figure adapted from Bastani et al. (2022) and modified from **Paper III**.

4.3.3 The field site

The study area (Fig. 4.5) is located in Stockholm, Sweden. The goal of the survey was to obtain a subsurface model below parts of the Lake Mälaren to investigate the geology for a tunnel project planned by the Swedish Transport Administration. Within two field surveys, RMT data were collected on a boat and CSEM data were obtained in winter on the frozen lake. Both data sets were evaluated with 2-D inversion approaches in Bastani et al. (2015), Mehta et al. (2017) and Bastani et al. (2022). In the study area, major parts of the rocks are granitic to granodioritic and deformation zones are present (Persson, 2002). Drilling logs in the area reveal that the bedrock is frequently fractured by brittle deformation and that the fractures are often filled with conductive minerals (Mehta et al., 2017). Besides verifying the inversion code, the 3-D resistivity model in this work confirms the locations of conductive anomalies related to fracture zones, which are important to be taken into account during the construction of the planned tunnel.

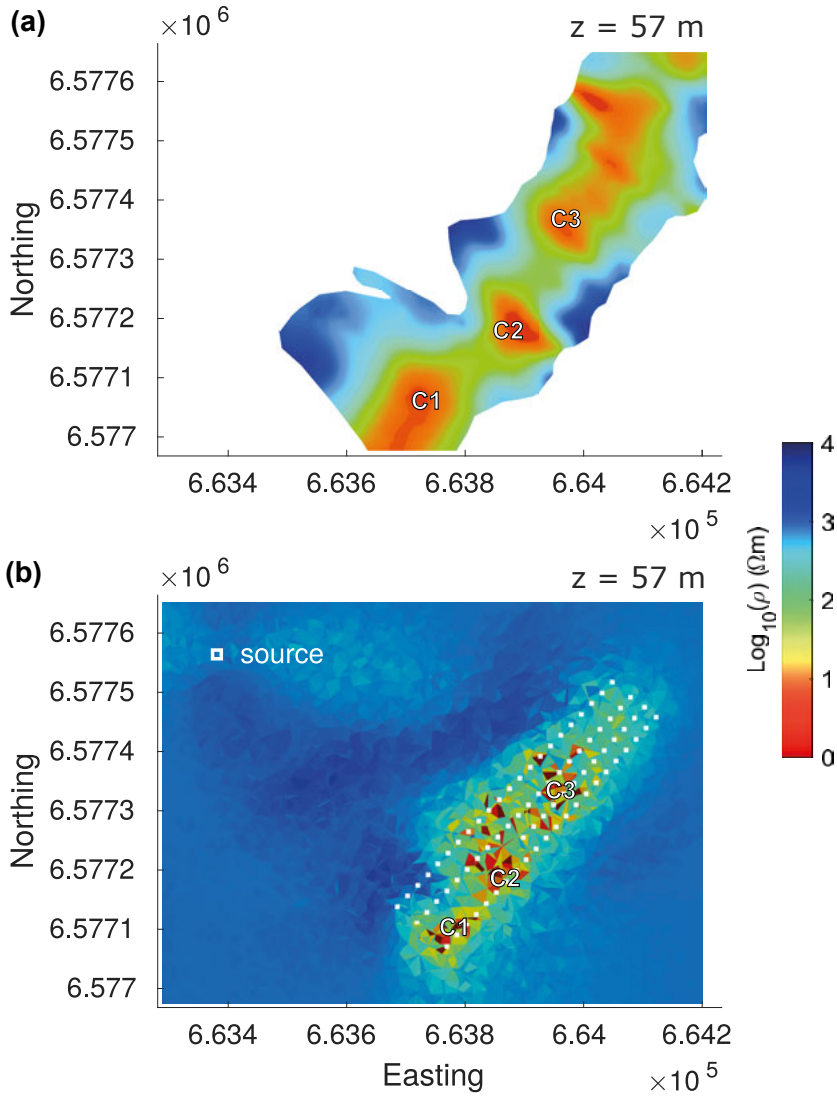


Figure 4.6. Resistivity depth-slices obtained from 2-D resistivity models (Mehta et al., 2017) computed with a determinant inversion approach of RMT data (a) and from 3-D CSEM inversion (b). Figure modified from **Paper III**. Data and data fit for the 3-D model are presented in **Paper III**.

4.4 Paper IV

A comparison between controlled-source electromagnetic field components and transfer functions as input data for three-dimensional non-linear conjugate gradient inversion

4.4.1 Motivation

When using EM field components as input data for CSEM inversion, the source currents must be provided for the calculations. However, it might be challenging to measure source current strength and phase in the field. The use of transfer functions in the form of impedance tensors and VMTF generated by two independent sources brings the advantage that source currents do not need to be known. On the one hand, information on the subsurface may be lost in the transfer function formulation of CSEM data (Zonge and Hughes, 1991; Sasaki et al., 2015). On the other hand, Bretaudeau and Coppo (2016) observed that the use of transfer functions can reduce the signature of the source in the resistivity models.

4.4.2 Summary

This paper is a research note that investigates the data gradient pattern, convergence behaviour and resistivity models of two inversion runs; one with field components and one with transfer functions as input data both using a synthetic model (Fig. 4.7) similar to the one studied in Sasaki et al. (2015).

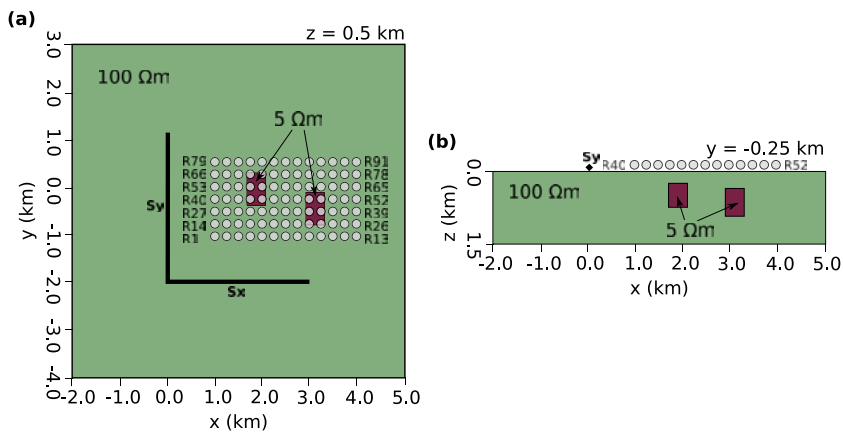


Figure 4.7. Synthetic model of **Paper IV**: horizontal (a) and vertical (b) slices through the inner model region. Circles and black lines indicate receiver stations (R1-R91) and two source cables (S_x , S_y) at the surface, respectively. Figure modified from **Paper IV**.

For this purpose, the NLCG inversion code discussed in **Paper III** was advanced to enable inversion of EM field components in addition to inversion of transfer function data. The results **Paper IV** indicate that both data types are well suited to detect the anomalies (Fig. 4.8), but the EM field component inversion recovers the true resistivities of the anomalies better. The convergence behaviour of the transfer function inversion is superior and the background resistivity is recovered more homogeneously with transfer functions than with field components as input data. While the sensitivity of the transfer function data is concentrated mainly below the receiver grid, field component data are also sensitive to the subsurface resistivity below the extended source, which introduces a source signature in the resistivity model.

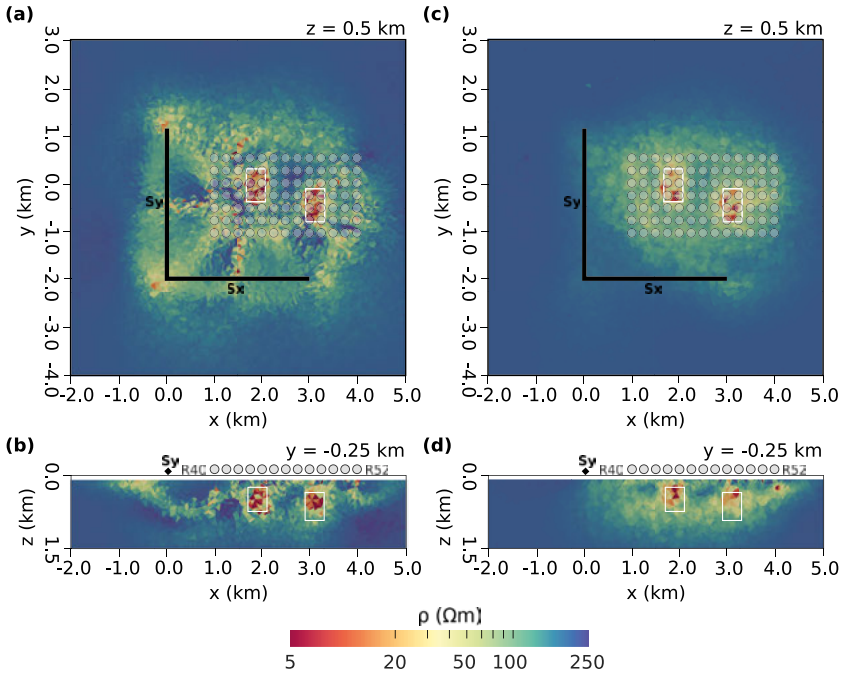


Figure 4.8. Inversion results of **Paper IV**: horizontal (a,c) and vertical (b,d) slices through the resistivity models obtained with EM field components (a, b) and impedance tensor and VMTF components (c, d). The outlines of the conductive anomalies (cf. Fig. 4.7) are depicted in white. Figure from **Paper IV**. Data and data fit are presented in **Paper IV**.

4.4.3 Remarks

The study of **Paper IV** is limited to one model and one inversion approach. In Example II of **Paper III** (Fig. 4.3), transfer functions are used as input data. Nevertheless, high data gradients and, therefore, artefacts in the resistivity model close to the source are observed. To reduce this source footprint, a distance-to-source weighting was introduced to the regularisation term. Consequently, it can be assumed that the use of transfer functions does not result in complete loss of sensitivity close to the source.

Furthermore, conclusions drawn in **Paper IV** might be limited to a measurement setup similar to the studied one. To formulate more comprehensive data evaluation recommendations, it is advised to study further measurement setups including i) near-field, transition and far-field zone measurements, ii) different types, numbers and sizes of transmitters and iii) semi-airborne measurement setups. Furthermore, comparing NLCG inversion to an inversion approach that utilises the full sensitivity matrix, i.e. a Gauss-Newton minimisation approach, should be tested in the future.

5. Conclusions and outlook

For this thesis, methods for 3-D CSEM forward and inverse modelling were implemented, adapted, applied and further developed. In the following, the main conclusions are drawn and outlooks on future development plans are devised.

Paper I presents the developed 3-D CSEM FE forward modelling code `elfe3D` and its mesh refinement options. The examined modelling examples demonstrate that the code produces accurate forward responses, creates optimised meshes and performs reasonably well.

To make the code more competitive, its accuracy and performance can be improved by implementing higher-order interpolation functions as well as more advanced boundary conditions and by including MPI parallelisation. The forward modelling code is included in the inversion framework `emilia` and the standalone version is planned to be made open-source.

Paper II investigates how the goal-oriented mesh refinement strategy of the forward modelling code can be applied in conjunction with high-order FE approximations to simulate models including steel infrastructure. The outcome is an improved understanding of mesh design for such models.

The presented modelling studies are limited to two scenarios with borehole casings modelled with a PEC approximation. Efforts should be made to examine how the PEC approximations behave within an inversion routine and if they influence the inversion result in any way.

Paper III reports on theoretical details and the verification of the further-developed NLCG inversion algorithm for 3-D models obtained with impedance tensor and VMTF input data. The examples demonstrate the application of the code to synthetic and real data from surface-based CSEM measurements. Without modifications, the code should also be suitable for offshore or airborne settings, which has to be tested in the future.

For further developments, the focus should be put into performance improvement and model assessment strategies. It can be recommended to implement a dual mesh approach, i.e. separating the forward modelling and inversion meshes, to reduce the number of model parameters while ensuring the accuracy of the forward responses. Furthermore, a graphical user interface to generate models, meshes and input files for the inversion would facilitate the application of the inversion code for a wider scientific community.

Paper IV compares two input data types for 3-D CSEM inversion: EM field components and transfer functions generated by a set of two independently oriented, extended electric bipole sources. While preliminary conclusions can be drawn from this research note, a more comprehensive study including the assessment of a variety of different measurement setups as well as a theoretical look at data sensitivities could provide fundamental recommendations regarding the evaluation of CSEM data generated by two source polarisations.

In conclusion, all presented papers contribute to address some of the challenges regarding 3-D EM modelling and inversion aforementioned in the introduction of this thesis. **Papers I** and **II** demonstrate methods and examples for improving the accuracy of the EM forward responses while minimising computational costs and for mesh design. The inversion code developed for **Papers III** and **IV** produces reliable 3-D subsurface models from CSEM data. The code is integrated in the inversion framework *emilia* and can be used by the academic community for non-commercial purposes upon request.

The international EM community has always benefited from the work and the statements of very experienced and knowledgeable members. Almost two decades ago, Avdeev (2005) wrote in his review paper: "The most important challenge that faces the EM community today (2005) is to convince software developers to put their 3-D EM forward and inverse solutions into the public domain, at least after some time. This would have a strong impact on the whole subject and the developers would benefit from feedback regarding the real needs of the end-users". Recently, Jones (2023) stated: "We simply are not going to have enough young, trained exploration geophysicists in the 2030s and 2040s to reach net zero by 2050". Although this thesis seems very technical at first glance, the outcomes of my PhD project, in terms of software as well as in terms of personal development, address both of the above statements.

Finally, I would like to point out that I consider it an honour to be given the opportunity to apply the skills I have acquired during my PhD for the benefit of society in the future. I am planning to contribute to powerful, flexible and openly available software packages, to train and educate students and to design impactful projects connecting countries, research and industry as well as application and software development perspectives aiming at addressing our societal needs with scientific solutions.

6. Plain language summary

The subsurface of our planet Earth consists of various materials. The subsurface materials differ in their composition, water saturation and pore space. Geophysical methods are applied for investigating the physical properties of the subsurface materials, i.e. rocks, and their distribution. The electrical conductivity (inverse of resistivity) is a physical property that describes how electric charges can move through a subsurface material when exposed to an applied electric field. Electromagnetic methods are frequently used to survey the electrical resistivity distribution within the Earth, i.e. to investigate the location of possible mineral deposits, groundwater, oil and gas reservoirs or geothermal water.

Electromagnetic geophysical data are recorded with geophysical instruments at the surface, in boreholes or in the air. The mathematical equations describing the physics behind an electromagnetic geophysical application, are often complicated and can therefore only be solved approximately. A forward modelling computer program calculates numerically approximated electromagnetic fields resulting from a model of the subsurface, such as the electrical resistivity distribution, and a certain measurement setup. To obtain resistivity models from measured electromagnetic data, a forward modelling program is used in combination with an inverse algorithm. The inverse algorithm computes a subsurface model that produces electromagnetic responses matching the measured data.

When evaluating electromagnetic data, one challenge is to account for full three-dimensional (3-D) measurement setups and subsurface scenarios. Therefore, this thesis seeks to report on the development of a 3-D forward modelling code for controlled-source electromagnetic data and its integration into an inversion framework to enable the computation of 3-D resistivity models of the subsurface. The code is applied to different geological settings: A forward modelling study above an iron ore deposit in central Sweden aims at finding an adequate receiver distribution for the measurements. In a second forward modelling project, subsurface models including steel-cased wells that are for example present in geothermal fields are investigated. Finally, data collected on a frozen lake in Stockholm for a tunnel-project are inverted.

The benefit of the conducted research is twofold: First, the developed computer programs can be used by the academic community to obtain improved resistivity models. Second, the reported models and field setups provide detailed information for measurement design and the material parameter distribution of the subsurface.

7. Sammanfattning - Swedish summary

Jordens undergrund består av olika material, som ofta samlas under begreppet sten. Stenar skiljer sig till exempel i fråga om mineralinnehåll i primärmaterial, vattenmättnad och porutrymme. Geofysiska metoder används för att undersöka de fysikaliska egenskaperna hos materialen i underjorden och deras fördelning i ett visst område och på djupet för att fastställa var eventuella mineralfyndigheter, grundvatten eller termiska vatten, olje- och gasreservoarer eller förkastningszoner ligger i underjorden. Elektrisk ledningsförmåga är en fysikalisk egenskap som beskriver hur elektriska laddningar kan förflytta sig genom ett material när det utsätts för ett elektriskt fält. Det elektriska ledningsförmåga mäts med elektromagnetiska metoder. Elektromagnetiska data registreras med magnetometrar och elektroder, vilka mäter såväl det elektriska som det magnetiska fältet på ytan, i borrhål eller i luften.

Utvärderingen av elektromagnetiska data innebär simulationen av det elektriska och magnetiska fältet på undersökningsområdet. Sådana simulationer av elektromagnetiska fälten utförs på datorn med ett förfarande som kallas framåtmodellering. De matematiska ekvationerna, som beskriver fysiken bakom elektromagnetiska fält är komplicerade och kan därför endast approximeras numerisk.

En viktig utmaning vid utvärdering av elektromagnetiska data är att ta hänsyn till kompletta tredimensionella (3-D) mätkonfigurationer och scenarier under jordytan. Därför har ett 3-D framåt-modelleringsprogram för en geofysisk metod med kontrollerad elektromagnetisk strömkälla (controlled-source electromagnetics, CSEM) utvecklats i det här arbete. Modelleringsprogrammet blev sedan integrerat i ett inverteringsprogram, som gör det möjligt att beräkna 3-D resistivitetsmodeller av underjorden.

Under mina doktorandstudier har jag tillämpat både framåtmodelleringen och inversionsprogrammet på olika geologiska förhållanden: Min första modellstudie på en malmfyndighet i Mellansverige syftade till att hitta en lämplig mottagarfördelning för mätningarna. I det andra modelleringsprojektet ingick teoretiska underjordiska modeller med borrhål med stålhöljen, såsom de som finns i geotermiska fält. Slutligen inverterade jag data som samlats in på en frusen sjö nära Stockholm för ett tunnelprojekt och jag kompletterade de tidigare erhållna 2-D-resistivitetsmodeller med en 3-D-modell. Resultaten från mitt doktorandprojekt är användbar inom forskningen, men även i mineralutvinning och infrastrukturprojekt: Datorprogrammet beräknar resistivitetsmodeller som används för att förstå geologiska strukturer. Dessutom ger mit doktorsarbete exempel på och detaljerad information om utförandet av mätningar och fördelning av lokala parametrar i underjorden.

8. Zusammenfassung - German summary

Der Untergrund unseres Planeten Erde besteht aus verschiedenen Materialien, die sich in Zusammensetzung, Wassersättigung und Porenraum unterscheiden. Geophysikalische Methoden werden eingesetzt, um die physikalischen Eigenschaften der Materialien im Untergrund und ihre Verteilung in einem bestimmten Gebiet und in der Tiefe zu untersuchen. Die elektrische Leitfähigkeit (der inverse elektrische Widerstand) ist eine physikalische Eigenschaft, die beschreibt, wie sich elektrische Ladungen durch ein Material bewegen können, wenn es einem angelegten elektrischen Feld ausgesetzt ist. Elektromagnetische Verfahren werden häufig eingesetzt, um die Lokation und Ausdehnung von elektrisch leitfähigen Materialien im Untergrund zu bestimmen und so Orte möglicher Mineralvorkommen, von Grundwasser oder thermalen Wässern, von Öl- und Gasreservoirs oder von Störungszonen zu erkunden.

Elektromagnetische geophysikalische Daten werden mit geophysikalischen Instrumenten an der Oberfläche, in Bohrlöchern oder in der Luft aufgezeichnet. Die mathematischen Gleichungen, die die Physik hinter einer elektromagnetischen geophysikalischen Anwendung beschreiben, sind oft kompliziert und können nur numerisch gelöst werden. Eine solche numerische Simulation elektromagnetischer Felder wird mit einem Verfahren durchgeführt, das als Vorwärtsmodellierung bezeichnet wird. Ein Vorwärtsmodellierungsprogramm berechnet die elektromagnetischen Felder, die sich aus einem Modell des Untergrunds, also der Verteilung der elektrischen Leitfähigkeit, und einem bestimmten Messaufbau, ergeben.

Bei der Auswertung elektromagnetischer Daten besteht eine große Herausforderung darin, vollständige dreidimensionale (3-D) Messanordnungen und Untergrundszenerarien zu berücksichtigen. In dieser Promotionsschrift wird daher über die Entwicklung eines 3-D Vorwärtsmodellierungsprogramms für elektromagnetische Daten mit kontrollierten Quellstrom und die Integration in ein Inversionssystem berichtet, das die Berechnung von 3-D Widerstandsmodellen des Untergrunds ermöglicht.

Während der Promotions wurde das Programm für verschiedene geologische Gegebenheiten angewendet: Meine erste Modellierungsstudie über einer Erzlagerstätte in Mittelschweden zielt darauf ab, eine geeignete Empfänger-Verteilung für die Messungen zu finden. In einem zweiten Modellierungsprojekt werden Untergrundmodelle mit stahlverkleideten Bohrlöchern, wie sie beispielsweise in geothermischen Feldern vorkommen, untersucht. Eine Inversion von Daten, die auf einem zugefrorenen See in Stockholm für ein Tunnelprojekt gesammelt worden waren, ergänzt bereits existierenden 2-D-Widerstandsmodelle durch ein 3-D-Modell.

Die Forschung, die ich während meiner Promotion durchgeführt habe, ist von Nutzen für Wissenschaftler, aber, durch den Anwendungsbezug zu Mineralerkundung und Infrastrukturprojekten, auch für die Gesellschaft: Erstens kann das Inversions-Computerprogramm von der akademischen Gemeinschaft verwendet werden, um verbesserte Modelle zu erhalten. Zweitens liefert die Arbeit Beispiele und detaillierte Informationen für Messdesign und lokale Parameterverteilung im Untergrund.

9. Acknowledgements

Transformative experience:
a radically new experience
that cannot be assessed in advance
Paul (2014)

I like to describe my PhD journey as a transformative experience: When I decided to accept the offer for the PhD position, I knew very little about what to expect and how I would be shaped by it. However, I am convinced that it was not the content of the work that influenced me the most, but the people who accompanied me.

Therefore, I would first and foremost like to express my gratitude to my main supervisor, Thomas Kalscheuer, for his trust and his valuable scientific advice along the journey. I am also thankful for the support by my other supervisors, Gunilla Kreiss, Roland Roberts and Mehrdad Bastani, especially towards the end of my PhD. Thank you all for making this experience a successful one.

It was an honour to be part of the Smart Exploration project. Thank you, Alireza Mahlemir, for having me on your project. The scientific discussions and personal exchange with colleagues at conferences and project meetings have greatly contributed to this work. Thank you, Lasse, for introducing the EM instruments to me during my early days in Uppsala.

Laura, I don't think I can find an appropriate way to express my deep gratitude to you. You were the one, who helped me prepare my move to Uppsala six years ago. You and Sebastian picked me up from the airport, you made me feel welcome here. Thanks for the awesome team work, our fruitful discussions, your support and, most importantly, the great free time together. Thank you for becoming my close friend. Thank you for everything.

Thank you, Michael, for being my colleague and friend. Thanks for fun Challenge classes, great field work, helpful scientific discussions and fun fika breaks. Thank you, George, for our friendship, for being a good travel partner to our project meetings, for our runs, for your advice and for our insightful conversations. Thank you, Joshi, for the awesome times when you were my house, garden and office mate, for fun moments and serious conversations. Thank you, Tatiana, for our rare but very enjoyable chats. Thank you, Lea, for joining me sometimes for Challenge. Thank you, Zibi, for your motivational and sensitive words at the right moments. Thank you, Andra, for our motivating conversations and your positive attitude.

Christian, Mateja, Freja and Mia & Ruth, Lars, Lotta and Finja & Laura, Sebastian and Marina & Jenny, Jan and Jonna & Rodolphe, Pauline and August: Thank you for our friendship, for sharing experiences and the joint adventures. I will miss you. A lot! A big thanks goes to all other people in Uppsala who have accompanied me along the way.

I would also like to express my deep gratitude to people I met before or along the way helping me with my scientific and personal development. Thank you, Ute, Oliver and the EM group at GFZ Potsdam, for awakening my interest in electromagnetics, mentoring me during my Bachelor and Master studies, introducing me to the EM community and suggesting me to do my Erasmus studies in Uppsala. Thank you, Octavio, for initiating our collaboration. Thank you, Celine, for mentoring me during the challenging Covid times. Thank you, Dieter, for expressing your interest in working with me already a few years ago. Thank you, Anne & Tobias for your motivation, constructive feedback and friendship.

I am deeply thankful to my dear friends I have met before I moved to Sweden for my PhD. I don't think it would have been so easy for me to find a new home here without you being by my side via phone and visits: Thank you Luisa H. for our long phone calls, your visit in Uppsala in my first summer, for the music, the runs, for your valuable perspectives. Thank you, Luisa v.A., for sharing your PhD life with me and letting me share mine with you, for your motivation and advice, for your visit in the grey time of the year. Thank you Phil, for being my dear friend and study partner in Potsdam and for the support along my PhD journey. Nico, thank you for awakening my interest in student engagement and organisational work early on and for your good advice. Thank you, Caro, for your visits and for painting the cover picture of this thesis. Thank you, Quynh, Laura T. and Joanne, for accompanying my journey since school and for always staying in touch. Thank you all for your friendship.

I would like to express my sincere gratitude to my family in Germany: Liebe Mama, lieber Papa, Danke, dass ihr mich habt gehen lassen, wenn auch mit einem traurigen und einem fröhlichen Auge. Danke, für das, was ihr mir ermöglicht habt und für das liebevolle Umsorgen eurer Enkeltochter. Danke, Hanna, für die erwachsene Verbundenheit, die wir mittlerweile teilen und für das Diskutieren der PhD-Erfahrungen. Ich möchte auch Eike, Holger und Lucie ganz herzlich danken, dafür, dass ihr uns in unseren Entscheidungen unterstützt und so wunderbar für unsere Tochter da seid.

Finally, it comes to the most difficult paragraph of this thesis. Because there are no words to describe how I feel about my own little family. Thank you both, Ronja and Thorben, for your support, for your love, for showing me every day what's truly important in life, for shaping me more than anyone or anything else could.

Paula Rulff, Uppsala, October 2023

References

- Abubakar, A., Habashy, T. M., Li, M., and Liu, J. (2009). Inversion algorithms for large-scale geophysical electromagnetic measurements. *Inverse Problems*, 25(12):123012.
- Ahrens, J., Geveci, B., and Law, C. (2005). ParaView: An end-user tool for large data visualization. In *Visualization Handbook*. Elsevier.
- Alappat, C., Basermann, A., Bishop, A. R., Fehske, H., Hager, G., Schenk, O., Thies, J., and Wellein, G. (2020). A recursive algebraic coloring technique for hardware-efficient symmetric sparse matrix-vector multiplication. *ACM Transactions on Parallel Computing*, 7(3):1–37.
- Amestoy, P. R., Duff, I. S., L’Excellent, J.-Y., and Koster, J. (2001). A fully asynchronous multifrontal solver using distributed dynamic scheduling. *SIAM Journal on Matrix Analysis and Applications*, 23(1):15–41.
- Ansari, S. and Farquharson, C. G. (2014). 3D finite-element forward modeling of electromagnetic data using vector and scalar potentials and unstructured grids. *Geophysics*, 79(4):E149–E165.
- Auken, E., Pellerin, L., Christensen, N. B., and Sørensen, K. (2006). A survey of current trends in near-surface electrical and electromagnetic methods. *Geophysics*, 71(5):G249–G260.
- Avdeev, D. B. (2005). Three-dimensional electromagnetic modelling and inversion from theory to application. *Surveys in Geophysics*, 26:767–799.
- Avdeev, D. B., Kuvshinov, A. V., Pankratov, O. V., and Newman, G. A. (1997). High-performance three-dimensional electromagnetic modelling using modified Neumann series. Wide-band numerical solution and examples. *Earth, Planets and Space*, 49(11-12):1519–1539.
- Bastani, M., Persson, L., Mehta, S., and Malehmir, A. (2015). Boat-towed radio-magnetotellurics - A new technique and case study from the city of Stockholm. *Geophysics*, 80(6):B193–B202.
- Bastani, M., Wang, S., Malehmir, A., and Mehta, S. (2022). Radio-magnetotelluric and controlled-source magnetotelluric surveys on a frozen lake: Opportunities for urban applications in Nordic countries. *Near Surface Geophysics*, 20(1):30–45.
- Becken, M., Nittinger, C. G., Smirnova, M., Steuer, A., Martin, T., Petersen, H., Meyer, U., Mörbe, W., Yogeshwar, P., Tezkan, B., Matzander, U., Friedrichs, B., Rochlitz, R., Günther, T., Schiffler, M., and Stolz, R. (2020). DESMEX: A novel system development for semi-airborne electromagnetic exploration. *Geophysics*, 85(6):E253–E267.
- Bollhöfer, M., Eftekhari, A., Scheidegger, S., and Schenk, O. (2019). Large-scale sparse inverse covariance matrix estimation. *SIAM Journal on Scientific Computing*, 41(1):A380–A401.
- Bollhöfer, M., Schenk, O., Janalik, R., Hamm, S., and Gullapalli, K. (2020). State-of-the-art sparse direct solvers. In Grama, A. and Sameh, A. H., editors, *Parallel*

- Algorithms in Computational Science and Engineering*, pages 3–33. Springer International Publishing.
- Bretaudeau, F. and Coppo, N. (2016). A pseudo-MT formulation for 3D CSEM inversion with a single transmitter. *Conference Paper at EMIW2016 in Chiang Mai (Thailand)*.
- Cai, H., Long, Z., Lin, W., Li, J., Lin, P., and Hu, X. (2021). 3D multinary inversion of controlled-source electromagnetic data based on the finite-element method with unstructured mesh. *Geophysics*, 86(1):E77–E92.
- Cao, M., Tan, H. D., and Wang, K. P. (2016). 3D LBFGS inversion of controlled source extremely low frequency electromagnetic data. *Applied Geophysics*, 13(4):689–700.
- Castillo-Reyes, O., de la Puente, J., and Cela, J. M. (2018). PETGEM: A parallel code for 3D CSEM forward modeling using edge finite elements. *Computers & Geosciences*, 119:126–136.
- Castillo-Reyes, O., Queralt, P., Marcuello, A., and Ledo, J. (2021). Land CSEM simulations and experimental test using metallic casing in a geothermal exploration context: Vallés basin (NE Spain) case study. *IEEE Transactions on Geoscience and Remote Sensing*, 60:1–13.
- Commer, M. and Newman, G. A. (2008). New advances in three-dimensional controlled-source electromagnetic inversion. *Geophysical Journal International*, 172(2):513–535.
- Constable, S. (2010). Ten years of marine CSEM for hydrocarbon exploration. *Geophysics*, 75(5):A67–A81.
- Constable, S. C., Parker, R. L., and Constable, C. G. (1987). Occam’s inversion: a practical algorithm for generating smooth models from electromagnetic sounding data. *Geophysics*, 52(3):289–300.
- Deleersnyder, W., Dudal, D., and Hermans, T. (2022). Novel airborne EM image appraisal tool for imperfect forward modeling. *Remote Sensing*, 14(22):5757.
- Dentith, M. and Mudge, S. T. (2014). *Geophysics for the Mineral Exploration Geoscientist*. Cambridge University Press.
- Elías, M. W., Zyserman, F. I., Rosas-Carbajal, M., and Manassero, M. C. (2022). Three-dimensional modelling of controlled source electro-magnetic surveys using non-conforming finite element methods. *Geophysical Journal International*, 229(2):1133–1151.
- European Environment Agency (2021). *Improving the climate impact of raw material sourcing*. Number 08.
- Fletcher, R. and Reeves, C. M. (1964). Function minimization by conjugate gradients. *The Computer Journal*, 7(2):149–154.
- Ghorbani, Y., Nwaila, G. T., Zhang, S. E., Bourdeau, J. E., Cánovas, M., Arzua, J., and Nikadat, N. (2023). Moving towards deep underground mineral resources: Drivers, challenges and potential solutions. *Resources Policy*, 80.
- Grayver, A. V. and Kolev, T. V. (2015). Large-scale 3D geoelectromagnetic modeling using parallel adaptive high-order finite element method. *Geophysics*, 80(6):E277–E291.
- Grayver, A. V., Streich, R., and Ritter, O. (2013). Three-dimensional parallel distributed inversion of CSEM data using a direct forward solver. *Geophysical Journal International*, 193(3):1432–1446.

- Grayver, A. V., Streich, R., and Ritter, O. (2014). 3D inversion and resolution analysis of land-based CSEM data from the Ketzin CO₂ storage formation. *Geophysics*, 79(2):E101–E114.
- Gribenko, A. and Zhdanov, M. (2007). Rigorous 3-D inversion of marine CSEM data based on the integral equation method. *Society of Exploration Geophysicists - SEG International Exposition and 76th Annual Meeting 2006, SEG 2006*, 72(2):815–819.
- Günther, T., Rücker, C., and Spitzer, K. (2006). Three-dimensional modelling and inversion of dc resistivity data incorporating topography - II. Inversion. *Geophysical Journal International*, 166(2):506–517.
- Haber, E., Ascher, U. M., and Oldenburg, D. W. (2004). Inversion of 3D electromagnetic data in frequency and time domain using an inexact all-at-once approach. *Geophysics*, 69(5):1216–1228.
- Hansen, P. C. and O’Leary, D. P. (1993). The use of the l-curve in the regularization of discrete ill-posed problems. *SIAM Journal on Scientific Computing*, 14(6):1487–1503.
- Heagy, L. J., Cockett, R., Kang, S., Rosenkjaer, G. K., and Oldenburg, D. W. (2017). A framework for simulation and inversion in electromagnetics. *Computers and Geosciences*, 107(June):1–19.
- Heagy, L. J. and Oldenburg, D. W. (2023). Impacts of magnetic permeability on electromagnetic data collected in settings with steel-cased wells. *Geophysical Journal International*, 234(2):1092–1110.
- Jin, J. (2014). *The Finite Element Method in Electromagnetics*. Wiley-IEEE Press, 3rd edition.
- Jones, A. G. (2023). Mining for net zero: The impossible task. *The Leading Edge*, 42(4):266–276.
- Kalscheuer, T., Blake, S., Podgorski, J. E., Wagner, F., Green, A. G., Muller, M., Jones, A. G., Maurer, H., Ntibinyane, O., and Tshoso, G. (2015). Joint inversions of three types of electromagnetic data explicitly constrained by seismic observations: results from the central Okavango Delta, Botswana. *Geophysical Journal International*, 202(3):1429–1452.
- Kalscheuer, T., Garcia Juanatey, M., Meqbel, N., and Pedersen, L. B. (2010). Non-linear model error and resolution properties from two-dimensional single and joint inversions of direct current resistivity and radiomagnetotelluric data. *Geophysical Journal International*, 182(3):1174–1188.
- Kalscheuer, T., Pedersen, L. B., and Siripunvaraporn, W. (2008). Radiomagnetotelluric two-dimensional forward and inverse modelling accounting for displacement currents. *Geophysical Journal International*, 175(2):486–514.
- Kara, K. B. and Farquharson, C. G. (2023). 3D minimum-structure inversion of controlled-source EM data using unstructured grids. *Journal of Applied Geophysics*, 209:104897.
- Kelbert, A., Meqbel, N., Egbert, G. D., and Tandon, K. (2014). ModEM: A modular system for inversion of electromagnetic geophysical data. *Computers and Geosciences*, 66:40–53.
- Keller, G. (1982). Rock and Mineral Properties. In *Carmichael, R. S., (Ed.), Handbook of Physical Properties of Rocks*. CRC Press, 1st edition.

- Keller, G. (1987). Rock and Mineral Properties. In M. C. Nabighian, (Ed.), *Electromagnetic Methods in Applied Geophysics: Part A*, pages 13–52. Tulsa, OK: Society of Exploration Geophysicists, 1st edition.
- Key, K. (2016). MARE2DEM: A 2-D inversion code for controlled-source electromagnetic and magnetotelluric data. *Geophysical Journal International*, 207(1):571–588.
- Lelièvre, P. G., Carter-McAuslan, A. E., Dunham, M. W., Jones, D. J., Nalepa, M., Squires, C. L., Tycholiz, C. J., Vallée, M. A., and Farquharson, C. G. (2018). Facetmodeller: Software for manual creation, manipulation and analysis of 3d surface-based models. *SoftwareX*, 7:41–46.
- Li, X. and Pedersen, L. B. (1991). Controlled source tensor magnetotellurics. *Geophysics*, 56(9):1456–1461.
- Liu, Z., Ren, Z., Yao, H., Tang, J., Lu, X., and Farquharson, C. (2023). A parallel adaptive finite-element approach for 3-D realistic controlled-source electromagnetic problems using hierarchical tetrahedral grids. *Geophysical Journal International*, 232(3):1866–1885.
- Long, Z., Cai, H., Hu, X., Li, G., and Shao, O. (2020). Parallelized 3-D CSEM inversion with secondary field formulation and hexahedral mesh. *IEEE Transactions on Geoscience and Remote Sensing*, 58(10):6812–6822.
- Mackie, R., Watts, M., and Rodi, W. (2007). Joint 3D inversion of marine CSEM and MT data. *Expanded Abstracts 77th Ann. Int. Meeting, SEG*.
- Mehta, S., Bastani, M., Malehmir, A., and Pedersen, L. B. (2017). Resolution and sensitivity of boat-towed RMT data to delineate fracture zones - Example of the Stockholm bypass multi-lane tunnel. *Journal of Applied Geophysics*, 139:131–143.
- Menke, W. (2012). Chapter 9 - nonlinear inverse problems. In Menke, W., editor, *Geophysical Data Analysis: Discrete Inverse Theory*, pages 163–188. Academic Press, Boston, 3rd edition.
- Moorkamp, M. (2017). Integrating electromagnetic data with other geophysical observations for enhanced imaging of the earth: A tutorial and review. *Surveys in Geophysics*, 38(5):935–962.
- Nabighian, M.N., e. (1987). *Electromagnetic Methods in Applied Geophysics*. Tulsa, OK: Society of Exploration Geophysicists, 1st edition.
- Newman, G. A. and Alumbaugh, D. L. (2000). Three-dimensional magnetotelluric inversion using non-linear conjugate gradients. *Geophysical Journal International*, 140(2):410–424.
- Newman, G. A. and Boggs, P. T. (2004). Solution accelerators for large-scale three-dimensional electromagnetic inverse problems. *Inverse Problems*, 20(6):S151.
- Oden, J. and Prudhomme, S. (2001). Goal-Oriented Error Estimation and Adaptivity for the Finite Element Method. *Computers and Mathematics with Applications*, 41:735–756.
- Oden, J. T. and Prudhomme, S. (1999). On goal-oriented error estimation for elliptic problems: application to the control of pointwise errors. *Computer Methods in Applied Mechanics and Engineering*, 176:313–331.
- Oldenburg, D. W., Heagy, L. J., Kang, S., and Cockett, R. (2020). 3D electromagnetic modelling and inversion: a case for open source. *Exploration Geophysics*, 51(1):25–37.

- Paasche, H. and Tronicke, J. (2014). Nonlinear joint inversion of tomographic data using swarm intelligence. *Geophysics*, 79(4):R133–R149.
- Patzner, C., Tietze, K., and Ritter, O. (2019). Elongated horizontal and vertical receivers in three-dimensional electromagnetic modelling and inversion. *Geophysical Prospecting*, 67(8):2227–2244.
- Paul, L. A. (2014). *Transformative Experience*. Oxford University Press.
- Persson, L. (2002). *Plane wave electromagnetic measurements for imaging fracture zones*. PhD thesis, Uppsala University.
- Plessix, R. E. and Mulder, W. A. (2008). Resistivity imaging with controlled-source electromagnetic data: Depth and data weighting. *Inverse Problems*, 24(3):034012.
- Polak, E. and Ribiere, G. (1969). Note sur la convergence de méthodes de directions conjuguées. *Revue française d'informatique et de recherche opérationnelle. Série rouge*, 3(R1):35–43.
- Puzyrev, V., Koldan, J., de la Puente, J., Houzeaux, G., Vázquez, M., and Cela, J. M. (2013). A parallel finite-element method for three-dimensional controlled-source electromagnetic forward modelling. *Geophysical Journal International*, 193(2):678–693.
- Ren, Z. and Kalscheuer, T. (2020). Uncertainty and resolution analysis of 2D and 3D inversion models computed from geophysical electromagnetic data. *Surveys in Geophysics*, 41(1):47–112.
- Ren, Z., Kalscheuer, T., Greenhalgh, S., and Maurer, H. (2013). A goal-oriented adaptive finite-element approach for plane wave 3-D electromagnetic modelling. *Geophysical Journal International*, 194(2):700–718.
- Reynolds, J. (2011). *An Introduction to Applied and Environmental Geophysics*. John Wiley and Sons Ltd, Chichester, England, 2nd edition.
- Rochlitz, R., Becken, M., and Günther, T. (2023). Three-dimensional inversion of semi-airborne electromagnetic data with a second-order finite-element forward solver. *Geophysical Journal International*, 234(1):528–545.
- Rochlitz, R., Skibbe, N., and Günther, T. (2019). CustEM: Customizable finite-element simulation of complex controlled-source electromagnetic data. *Geophysics*, 84(2):F17–F33.
- Rodi, W. and Mackie, R. L. (2001). Nonlinear conjugate gradients algorithm for 2-D magnetotelluric inversion. *Geophysics*, 66(1):174–187.
- Römhild, L., Sonntag, M., Kiyani, D., Rogers, R., Rath, V., and Börner, J. (2019). Anisotropic complex electrical conductivity of black shale and mudstone from the Moffat Shale Group (Ireland). *Near Surface Geophysics*, 17(6):675–690.
- Rücker, C. (2011). *Advanced electrical resistivity modelling and inversion using unstructured discretization*. PhD thesis, University of Leipzig.
- Saad, Y. (1994). SPARSEKIT: a basic tool kit for sparse matrix computations. *Software documentation*.
- Sasaki, Y., Yi, M. J., Choi, J., and Son, J. S. (2015). Frequency and time domain three-dimensional inversion of electromagnetic data for a grounded-wire source. *Journal of Applied Geophysics*, 112:106–114.
- Schaller, A., Streich, R., Drijkoningen, G., Ritter, O., and Slob, E. (2018). A land-based controlled-source electromagnetic method for oil field exploration: An example from the Schoonebeek oil field. *Geophysics*, 83(2):WB1–WB17.

- Schwarzbach, C., Börner, R. U., and Spitzer, K. (2011). Three-dimensional adaptive higher order finite element simulation for geo-electromagnetics-a marine CSEM example. *Geophysical Journal International*, 187(1):63–74.
- Shewchuk, J. R. (1994). An introduction to the conjugate gradient method without the agonizing pain. Technical report, Carnegie Mellon University, USA.
- Si, H. (2015). Tetgen, a delaunay-based quality tetrahedral mesh generator. *ACM Transactions on Mathematical Software*, 41(2):1–36.
- Si, H. (2020). *TetGen. A Quality Tetrahedral Mesh Generator and 3D Delaunay Triangulator*. Available at <http://www.tetgen.org>.
- Smirnova, M., Shlykov, A., Asghari, S. F., Tezkan, B., Saraev, A., Yogeshwar, P., and Smirnov, M. (2023). 3D controlled-source electromagnetic inversion in the radio-frequency band. *Geophysics*, 88(1):E1–E12.
- Spitzer, K. (2023). Electromagnetic modeling using adaptive grids - error estimation and geometry representation. *Surveys in Geophysics*, pages 1–38.
- Streich, R. (2016). Controlled-source electromagnetic approaches for hydrocarbon exploration and monitoring on land. *Surveys in Geophysics*, 37(1):47–80.
- Streich, R. and Swidinsky, A. (2023). On method-of-moments modelling of electromagnetic sources connected to metallic well casings. *Geophysical Journal International*, 234(2):1476–1483.
- Telford, W., Geldart, L., and Sheriff, R. (1990). *Applied Geophysics*. Cambridge University Press, Cambridge, 770, 2nd edition.
- Tietze, K., Ritter, O., Patzer, C., Veeken, P., and Dillen, M. (2019). Repeatability of land-based controlled-source electromagnetic measurements in industrialized areas and including vertical electric fields. *Geophysical Journal International*, 218(3):1552–1571.
- Tietze, K., Ritter, O., and Veeken, P. (2015). Controlled-source electromagnetic monitoring of reservoir oil saturation using a novel borehole-to-surface configuration. *Geophysical Prospecting*, 63(6):1468–1490.
- Tikhonov, A. N. and Arsenin, V. I. (1977). *Solutions of ill-posed problems*. Scripta series in mathematics. Winston; New York: distributed solely by Halsted Press, Washington.
- Um, E. S., Kim, J., and Wilt, M. (2020). 3D borehole-to-surface and surface electromagnetic modeling and inversion in the presence of steel infrastructure. *Geophysics*, 85(5):E139–E152.
- Ward, S. H. and Hohmann, G. (1988). Electromagnetic Theory for Geophysical Applications. In M. C. Nabighian, (Ed.), *Electromagnetic Methods in Applied Geophysics: Part A*, pages 131–311. Tulsa, OK: Society of Exploration Geophysicists, 1st edition.
- Weiss, M., Kalscheuer, T., and Ren, Z. (2023a). Spectral element method for 3-D controlled-source electromagnetic forward modelling using unstructured hexahedral meshes. *Geophysical Journal International*, 232(2):1427–1454.
- Weiss, M., Neytcheva, M., and Kalscheuer, T. (2023b). Iterative solution methods for 3D controlled-source electromagnetic forward modelling of geophysical exploration scenarios. *Computational Geosciences*, 27:81–102.
- Werthmüller, D., Mulder, W. A., and Slob, E. C. (2019). emg3d: A multigrid solver for 3D electromagnetic diffusion. *Journal of Open Source Software*, 4(39):1463.

- Werthmüller, D., Rochlitz, R., Castillo-Reyes, O., and Heagy, L. (2021). Towards an open-source landscape for 3-D CSEM modelling. *Geophysical Journal International*, 227(1):644–659.
- Zbinden, D. (2015). Inversion of 2D magnetotelluric and radiomagnetotelluric data with non-linear conjugate gradient techniques. Master’s thesis, Uppsala University.
- Zhang, B., Yin, C., Han, X., Wang, L., Liu, Y., Ren, X., Su, Y., and Chand Baranwal, V. (2023). Three-Dimensional Airborne Electromagnetic Data Inversion With Flight Altitude Correction. *IEEE Transactions on Geoscience and Remote Sensing*, 61:5910610.
- Zhang, Y. (2018). *Parallel goal-oriented adaptive finite element modeling for 3D electromagnetic exploration*. PhD thesis, University of California San Diego.
- Zhdanov, M. (2009). *Geophysical Electromagnetic Theory and Methods*. Elsevier.
- Zhdanov, M. S. (2002). *Geophysical Inverse Theory and Regularization Problems*, volume 36 of *Methods in Geochemistry and Geophysics*. Elsevier.
- Zonge, K. L. and Hughes, L. J. (1991). Controlled source audio-frequency magnetotellurics. In *Electromagnetic Methods in Applied Geophysics: Volume 2, Application, Parts A and B*. Society of Exploration Geophysicists.

Acta Universitatis Upsaliensis

Digital Comprehensive Summaries of Uppsala Dissertations from the Faculty of Science and Technology 2331

Editor: The Dean of the Faculty of Science and Technology

A doctoral dissertation from the Faculty of Science and Technology, Uppsala University, is usually a summary of a number of papers. A few copies of the complete dissertation are kept at major Swedish research libraries, while the summary alone is distributed internationally through the series Digital Comprehensive Summaries of Uppsala Dissertations from the Faculty of Science and Technology. (Prior to January, 2005, the series was published under the title "Comprehensive Summaries of Uppsala Dissertations from the Faculty of Science and Technology".)



Distribution: publications.uu.se
urn:nbn:se:uu:diva-514339

ACTA UNIVERSITATIS
UPSALIENSIS
2023